**THESIS FOR THE DEGREE OF DOCTOR OF PHILOSOPHY**

# Laser powder bed fusion of 316L stainless steel

## Microstructure and mechanical properties as a function of process parameters, design and productivity

ALEXANDER LEICHT


CHALMERS

Department of Industrial and Materials Science
CHALMERS UNIVERSITY OF TECHNOLOGY
Gothenburg, Sweden 2020

Laser powder bed fusion of 316L stainless steel
Microstructure and mechanical properties as a function of process parameters, design and productivity

Alexander Leicht
ISBN 978-91-7905-289-8



Doctoral thesis at Chalmers University of Technology
New serial no: 4756
ISSN 0346-718X

Department of Industrial and Materials Science
Chalmers University of Technology
SE-412 96 Gothenburg
Sweden
Telephone + 46 (0)31-772 1000
URL: www.chalmers.se

Cover photo: Electron backscatter image in three different orientations of a stainless steel 316L sample produced with laser powder bed fusion.

Printed by Chalmers Digitaltryck
Gothenburg, Sweden 2020

# Laser powder bed fusion of 316L stainless steel

Microstructure and mechanical properties as a function of process parameters, design and productivity

ALEXANDER LEICHT
Department of Industrial and Materials Science
Chalmers University of Technology

## Abstract

One of the most common additive manufacturing techniques for fabricating metallic components is laser powder bed fusion, which has demonstrated great potential in fabricating parts with properties exceeding the properties achieved via conventional methods. To fully utilize the process's potential, a more profound understanding of the microstructure and properties of the laser powder bed fusion processed material is required. This thesis aims to provide new insights into how the microstructure, mechanical properties and productivity are affected by part design and process parameters. The thesis is framed around a detailed investigation of the parts produced in stainless steel 316L.

The provided results reveal that producing parts with standard process parameters leads to near-full density with excellent tensile properties and a microstructure consisting of large elongated grains with predominant <101> orientation characterized by a fine submicron cellular structure. It was demonstrated that part thickness does not influence component density, but the grain morphology and texture are affected close to the part edges. Reducing the part thickness to less than 0.5 mm reduced the predominant texture and reducing the part thickness to less than 1 mm reduced the yield strength.

Altering the process parameters affected the crystallographic orientation, grain size and cell size and thus the tensile properties. Minor effects of processing gas composition (Ar, $N_2$ or He) on the chemical composition, microstructure, tensile strength and hardness was detected.

In addition, it was revealed that a 20% faster build time could be achieved without compromising the static properties by adjusting the scan speed and hatch distance. Increasing the layer thickness to 80 μm allowed for shortening the build time by a factor of four but with a 14% reduction in yield strength and 17% reduction in ductility.

The findings provided in this thesis serve as a basis for the development of rules for part design and qualification of mechanical properties for manufacturing parts with fine design features via laser powder bed fusion. The results emphasize the importance of the part design on the microstructure and the properties of the produced component. In addition, the presented results emphasize the potential for significant improvement in build speed in the laser powder bed fusion process, exemplified for 316L.

**Keywords:** additive manufacturing, laser powder bed fusion, stainless steel, 316L, thin-wall structures, microstructure, design for additive manufacturing, productivity, tensile properties

# Preface

This work was conducted at the Department of Industrial and Materials Science, Chalmers University of Technology (Gothenburg, Sweden) under the supervision of Prof. Eduard Hryha and Prof. Uta Klement between June 2015 and May 2020. The examiner was Prof. Lars Nyborg.

The focus of this thesis is on the design, productivity and properties of stainless steel 316L parts manufactured via laser powder bed fusion. The design-related work concerns how different designs affect the microstructure and mechanical properties of fabricated parts. In terms of productivity, the focus is placed on developing a set of process parameters that increases the build speed while still providing mechanical performance that fulfills specific requirements.

The thesis consists of an introductory part followed by the appended papers listed below:

**I.** **Effect of build geometry on the microstructural development of 316L parts produced by additive manufacturing**
*A. Leicht, U. Klement, E. Hryha*
*Mater. Charact. 143 (2018) 137–143*

**II.** **Effect of part thickness on the microstructure and mechanical properties of 316L parts produced by laser powder bed fusion**
*A. Leicht, C. Pauzon, M. Rashidi, U. Klement, L. Nyborg, E. Hryha*
*Submitted for publication*

**III.** **Effect of the process gas and scan speed on the properties and productivity of thin 316L structures produced by L-PBF**
*C. Pauzon, A. Leicht, U. Klement, P. Forêt, E. Hryha*
*Submitted for publication*

**IV.** **Effect of scan rotation on the microstructure development and mechanical properties of 316L parts produced by laser powder bed fusion**
*A. Leicht, C.H Yu, V. Luzin, U. Klement, E. Hryha*
*Mater. Charact. 163 (2020) 110309*

**V.** **Effect of process parameters on the microstructure, tensile strength and productivity of 316L parts produced by laser powder bed fusion**
*A. Leicht, M. Rashidi, U. Klement, E. Hryha*
*Mater. Charact. 159 (2020) 110016*

**VI.** **Increasing the productivity of laser powder bed fusion for 316L through increased layer thickness: Effect on microstructure and mechanical properties**
*A. Leicht, M. Fischer, U. Klement, E. Hryha, L. Nyborg*
*Submitted for publication*

## Contribution to the appended papers

**I.** The author planned and performed the experimental work and analysis of the results in collaboration with the co-authors. The author wrote the article in close cooperation with the co-authors.

**II.** The author planned and performed the experimental work and analysis in collaboration with C. Pauzon. The author wrote the article in cooperation with the co-authors.

**III.** The author planned and performed the experimental work and analysis in collaboration with the co-authors. The author wrote the EBSD section of the paper.

**IV.** The author planned the paper and performed most of the experimental work and analysis. Neutron diffraction measurements were performed and evaluated by C.H. Yu. The author wrote the article in cooperation with the co-authors.

**V.** The author planned and performed the experimental work and analysis in collaboration with the co-authors. The author wrote the paper in cooperation with the co-authors.

**VI.** The author planned and performed the experimental work and analysis in collaboration with the co-authors. The author wrote the paper in cooperation with the co-authors. The melt pool monitoring results were evaluated and summarized by M. Fischer.

## Papers not appended in this thesis

**A. Characterization of virgin and recycled 316L powder used in additive manufacturing**
*A. Leicht, R. Shvab, E. Hryha, L. Nyborg, L.-E. Rännar*
*Conference proceeding of SPS16, Lund, Sweden 2016*

**B. As-HIP Microstructure of EBM Fabricated Shell Components**
*A. Leicht, M. Vattur Sundaram, E. Hryha, L. Nyborg, M. Ahlfors, L.-E. Rännar, K. Frisk*
*Conference proceeding of World PM 2016, Hamburg, Germany 2016*

**C. Characterization Of The Virgin And Re-cycled Nickel Alloy HX Powder Used For Selective Laser Melting**
*R. Shvab, A. Leicht, E. Hryha, L. Nyborg*
*Conference proceeding of World PM 2016, Hamburg, Germany 2016*

**D. Surface Oxide State on Metal Powder and its Changes during Additive Manufacturing: an Overview**
*E. Hryha, R. Shvab, H. Gruber, A. Leicht, L. Nyborg*
*Proceeding of Euro PM 2017 Congress & Exhibition, Milan, Italy 2017*

**E. Constraint replacement-based design for AM of satellite components: ensuring design manufacturability through tailored test artefacts**
*O. Borgue, J. R. Müller, A. Leicht, M. Panarotto, O. Isaksson*
*Aerospace,* 2019, *6*, 124.

# CONTENTS

# Abbreviations

| | |
|---|---|
| AB | As-built |
| AM | Additive manufacturing |
| ASTM | American Society for Testing and Materials |
| BCC | Body-centered-cubic |
| BD | Build direction |
| BSE | Backscattered electrons |
| CAD | Computer-aided design |
| E% | Elongation at break |
| EBSD | Electron backscatter diffraction |
| EDX | Energy-dispersive X-ray spectroscopy |
| FCC | Face-centered-cubic |
| HAGB | High-angle grain boundaries |
| HIP | Hot isostatic pressing |
| HT | Heat-treated |
| ISO | International Organization for Standardization |
| KAM | Kernel average misorientation |
| LOM | Light optical microscopy |
| L-PBF | Laser powder bed fusion (also known as laser based powder bed fusion) |
| PSD | Particle size distributions |
| SE | Secondary electrons |
| SEM | Scanning electron microscopy |
| STL | Stereo-lithography |
| UTS | Ultimate tensile strength |
| XRD | X-ray diffraction |
| YS | Yield strength |

# CHAPTER 1

## INTRODUCTION

The constant effort to improve product performance has inspired engineers and designers to develop more innovative parts; however, they are often burdened by the limitations of the manufacturing processes. These limitations serve as primary motivators for the development of additive manufacturing, as it allows for nearly unlimited design possibilities (e.g., topology-optimized lattice structures [1]). Additive manufacturing provides new possibilities for product development, both as a tool for making prototypes and for the fabrication of high-end fully functional parts with advanced geometrical design. A well-adapted additive manufacturing process to produce metal components is laser powder bed fusion (L-PBF), a process considered to have good reproducibility for a number of qualified alloys. However, to fully utilize the opportunities offered by L-PBF, more profound knowledge concerning the process is needed to identify both the new possibilities and the limitations.

Many metal additive manufacturing processes initially struggled with inferior part quality that satisfied only limited demands. A tremendous amount of research and development has been conducted in the area of hardware and process parameter development until now. The main aim has been to reduce the porosity and increase the mechanical performance of the produced parts. Indeed, it has been demonstrated that components can be fabricated with properties equal to and even exceeding those achieved via conventional methods [2], although the effect of sample geometry has so far hardly been considered. Therefore, the understanding of how variations in geometrical design affect the microstructure and mechanical properties remains limited. Without such knowledge, components are designed without a proper understanding of how the design influences the outcome. This implies that more information and accurate results are needed for material models and topological optimizations to be meaningful and correct.

The L-PBF process uses a set of system settings, known as process parameters. The selection of the process parameters largely influences the part outcome (such as the microstructure and mechanical properties) and productivity. It has been demonstrated that the change in process parameters can create a wide range of microstructures and resulting mechanical properties [3–7]. The possibility to locally change the process parameters enables the production of complex multi-functional components with a locally designed microstructure and properties, which indeed is an appealing feature. Still, to be accessible for engineers and product developers, more research is needed to establish the link between the process parameters, microstructure and productivity. Furthermore, to be applicable, the correlation between a specific microstructure and the corresponding properties must be established.

Many of the available additive manufacturing technologies are limited due to their low productivity compared with traditional processes. As an estimation, a few dozens of $mm^3/h$ of material can be fabricated by L-PBF [8], which is lower by order of magnitude than what can be achieved by many conventional methods, such as casting and forging. This has led to an overall assumption that additive manufacturing should be used only for producing complex parts in low volumes. Furthermore, this is why most of the developments so far have occurred in sectors in which the price sensitivity and production volumes are relatively low (e.g., aerospace and medical applications). The low productivity in conjunction with high raw material costs have been identified as the main barriers for expanding to more price-sensitive sectors, such as the automotive industry [9]. Traditionally, the production cost increases with increased part complexity, while additive manufacturing has shown to have a more or less constant part cost. This is schematically illustrated in **Figure 1a**, in which additive manufacturing is compared with conventional methods [10]. The figure implies that part complexity should be high to obtain the maximum benefit from additive manufacturing. Furthermore, as illustrated in **Figure 1b**, the cost per part does not decrease with the volume of production to the same extent as is the case of many conventional methods. This suggests that the production volumes should remain low. Nevertheless, by increasing the production rate for complex structures, new business opportunities for additive manufacturing can be created in which higher component value would be realized by, for example, increasing part performance.

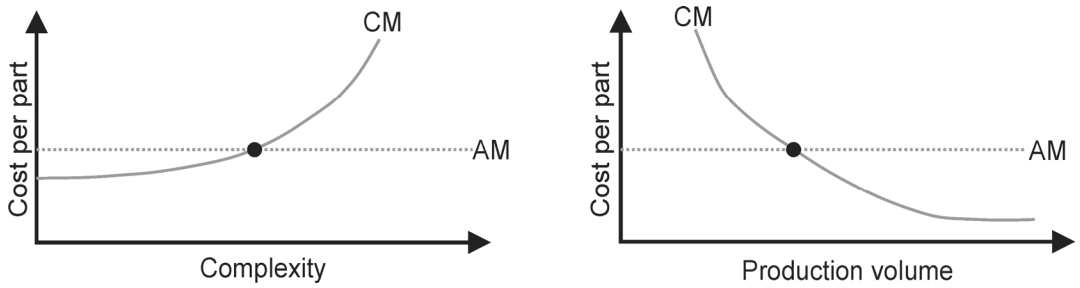


*Figure 1: Schematic correlation between the part cost for conventional manufacturing (CM) and additive manufacturing (AM) as a function of (a) complexity and (b) production volume. The black dot indicates the breakeven point in both cases, re-drawn from* [10].

## 1.1 Objectives

The focus of this thesis is framed around the laser powder bed processing of austenitic stainless steel 316L. The aim is to improve the knowledge of how the microstructure, mechanical properties and productivity are affected by the part design and process parameters. The objectives are summarized in the following research questions (RQ):

**RQ 1:** How does the part design affect the microstructure and mechanical properties?

**RQ 2:** How do the processing parameters affect the microstructure and mechanical properties?

**RQ 3:** How can productivity be improved without compromising the mechanical properties?

## 1.2 Research approach

The presented research is based on a detailed investigation of 316L parts produced with a laser powder bed fusion process applying different process parameters and design features. The results pertaining to the microstructure development provided a more qualitative and semi-quantitative evaluation of the L-PBF process-microstructure relationship, while the mechanical properties evaluation provided a more quantitative basis for results implementation. The research approach used in this thesis is schematically summarized in **Figure 2** and is elaborated in detail below.

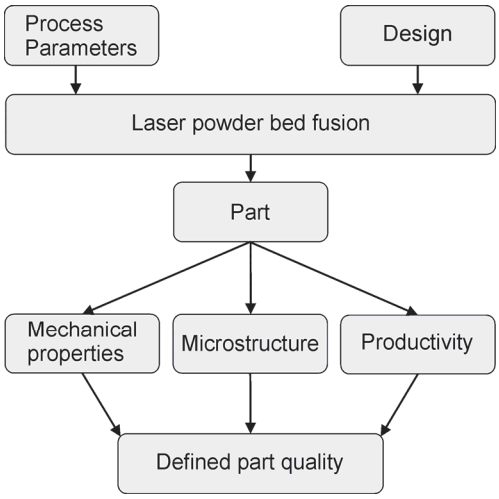


*Figure 2: Schematic illustration of the research approach with focus areas and the outcome.*

First, standard tensile test bars were produced with process parameters provided by the machine supplier (i.e., standard process parameters). The samples were evaluated to provide a solid baseline that could be used as a reference point for the appendant papers.

The primary objective and approach addressed by the different papers can be summarized as follows: Paper I investigates the differences in microstructure between samples produced with different thicknesses ranging from 3 mm to 0.2 mm. Paper II demonstrates the difference in tensile properties obtained by changing the part thickness from 3 mm to 1 mm. In Paper III, samples were produced in three different process gases (argon, nitrogen and helium) to evaluate the effect of the processing gas on the chemical composition, microstructure and mechanical properties. Then, Paper IV examines the outcome of four different scan rotations on the microstructure and mechanical properties. The effect of two of the main process parameters (i.e., hatch distance and scan speed) was investigated in Paper V to determine the effect on the microstructure, tensile strength and productivity. Finally, Paper VI studies the consequence of increasing the layer thickness from 20 µm to 80 µm on the microstructure, tensile strength and productivity. All the results used in Papers I–VI were obtained on samples produced with a stainless steel 316L powder on the same laser powder bed fusion machine.

# CHAPTER 2

## ADDITIVE MANUFACTURING OF METALS

A variety of technologies exist for the additive manufacturing of metals, such as binder jetting, directed energy deposition, sheet lamination and powder bed fusion [11]. There are differences between these technologies yet also some similarities. In this chapter, some of the possibilities are presented and associated with different sectors that have found additive manufacturing to be applicable.

The primary motivation for using additive manufacturing as a manufacturing technique has been to increase the part performance via design optimization. For example, in the aerospace industry, additive manufacturing has been used for producing turbine parts and lightweight cabin interiors, as illustrated in **Figure 3**.

In the medical industry, two well-established applications of additive manufacturing are medical implants, especially customized implants, and specialized surgical tools [12]. The possibility of mass customization has made it possible to produce patient-specific medical implants, which reduce the risk for health implications [13].

In the automotive industry, additive manufacturing is primarily used for producing functional prototypes. For utilizing additive manufacturing in mass production, the fabrication of parts is too slow and expensive at this stage; however, some sports and racecar manufactures have identified parts that are worthwhile to be produced by additive manufacturing, such as turbochargers [14].

Beyond these core sectors, manufacturing companies have indicated that tool fabrication is both costly and time consuming, which could potentially be circumvented via additive manufacturing. Again, the main benefits are associated with possibilities for novel designs and reduced lead times [15].

*Figure 3: A topologically optimized bracket for an aerospace application produced at Chalmers using a design developed with the aid of Simufact Additive simulations.*

Most industries have similar reasoning for using additive manufacturing, and these benefits, together with the associated limitations, are summarized in **Table 1**. Based on **Table 1** it appears that the benefits of additive manufacturing are best utilized when using it for the production of small intricate parts, in which the design can be improved to increase performance. The part should be made in a near-net shape, with a relatively low production volume. Design features such as thin walls are desired, as they would reduce both the weight and build time. In addition, the design should be optimized for additive manufacturing to decrease the build time and the need for post-processing (e.g., removal of support structures).

*Table 1: Some of the benefits and limitations associated with additive manufacturing of metals* [10].

| Benefits | Limitations |
|---|---|
| • Increased design freedom<br>• Shorter production cycles<br>• Potential for lightweight structures (e.g., lattice structures)<br>• New functions can be employed (e.g., internal cooling channels)<br>• Net-shaped production with lower material waste can be achieved | • Build volume limits the part size<br>• Number of available materials is limited<br>• Production volume is restricted by build speed<br>• Design freedom is limited by the necessity of support structures<br>• Post-processing is required (e.g., removal of support structures) |

# CHAPTER 3

# LASER POWDER BED FUSION

## 3.1 Process overview

**Figure 4** presents a schematic overview of the laser powder bed fusion process (L-PBF), highlighting the most vital components. The process involves the use of a high-quality laser beam guided onto the powder bed using mechanically movable mirrors. The L-PBF process is typically performed at elevated temperatures, between 60 and 200°C, created by maintaining the build plate at a given temperature. Additionally, during printing, the build chamber is filled with an inert or noble gas to minimize the oxidation of both the parts and the surrounding powder. The processing gas is regulated using an oxygen sensor located at the top of the machine that maintains the oxygen content at ~0.1% by adding more inert gas when needed.

During L-PBF, the powder layers are spread by a recoater blade, which can be made using various materials, such as steel, ceramic, carbon brush or rubber. Each recoater blade material has different advantages and is selected based on several aspects (e.g., part design, required tolerances and material, among others). To achieve good spreadability, the powder should be spherical, with a low number of satellites and a good particle size distribution. The L-PBF is associated with high material utilization; hence, to facilitate this, the un-melted powder is collected and reused after each build.

Recent developments have made to real-time monitoring systems, in which cameras and sensors provide in-situ monitoring of the state of both the powder bed and the melt pool. These systems allow for parameter adjustments and provide data that can be used to evaluate the effect of process parameters and design features once the build is complete.

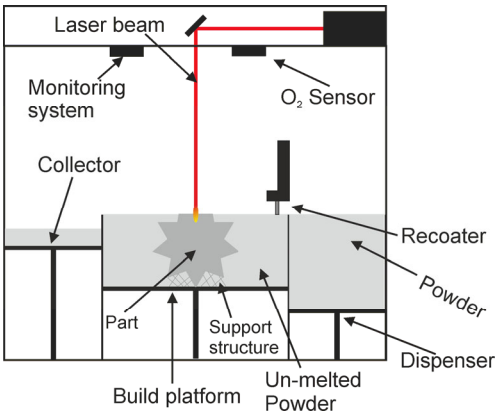


*Figure 4: Schematic overview of an L-PBF machine.*

Workflow in the case of L-PBF can be described as follows. Initially, the part must be designed and optimized for additive manufacturing using a 3D CAD software. The CAD representation of the part is then converted to an STL format [16], which is based on a triangular representation of the part. As different CAD software represent the part in different ways, the conversion to STL generates consistency in part representation. The STL file is then imported to a specialized software for part preparation for additive manufacturing (e.g., Materialise Magics), in which the part can be placed on the build plate, its build orientation be defined and the support structures be added. Both part and support structures are then exported to a machine-specific software in which the structures are further sliced into thin cross-sectional layers and the process parameters are set. Finally, the build job is transferred to the machine. Once the build job has been transferred to the machine, the component can begin to be built.

The build initiates by manually filling the machine with powder, leveling the build plate and finally applying the first powder layer onto a build plate. This is the last step in starting a build that requires manual labor. When the build is completed, the un-melted powder is vacuumed and sieved. The post-processing is typically completed manually and involves removing un-melted powder from the part, stress relief treatment, detaching the part from the build plate, and then removing the support structures. Removing the support structures, depending on complexity, can require much manual work. Depending on the application, heat treatments such as tempering, solution annealing, stress relief and hot isostatic pressing (HIP) might also be required. Some post-processing may also involve abrasive finishing, such as blasting and polishing, to smoothen the relatively rough as-built surface.

It has been estimated that up to 45% of the part cost during L-PBF is due to this pre- and post-processing [17]. This assumes, however, that a part design will be produced only once. If the part is instead developed specifically for additive manufacturing, this cost can be noticeably reduced. In the event that the part is designed for serial production, most of the pre-processing operations must be performed only once. Additionally, if the part has been designed with additive manufacturing in mind, its dimensions and orientation can be optimized to reduce the number of support structures required, again noticeably reducing the overall part costs. This would increase the production capacity and could further justify the high initial investment costs of the L-PBF process.

## 3.2 Process parameters

To achieve good process repeatability, control of the process and feedstock material is required. Significant research and development efforts have been made to produce high-quality parts (e.g., low weight, good strength and high accuracy) [2]. It has been demonstrated that the process parameters that most influence the quality are laser-related parameters, such as the power, scan speed, hatch distance and layer thickness [18–22]. This could also be why a large portion of the available research has focused on the process development, involving the analysis and correlation of these parameters to part quality and microstructure. Other parameters, such as the build plate temperature, recoater speed and process atmosphere, among others, might still be important but have been less studied. The following section explains the main process parameters and scanning strategies.

The scan speed is defined as the velocity of movement of the laser beam, while the scan vector (also known as the scan track) is the direction of the laser beam. It should be noted that some

L-PBF processes use a pulsed laser beam rather than a continuous laser beam. If a pulsed laser is used, then the time at each point translates to the scan speed.

The melting process begins when the laser beam, with a spot size of 100–150 µm in diameter, interacts with the powder, and the powder is heated by radiation well above the melting point, thereby forming a pool of liquid metal. In **Figure 5a and b,** a schematic melt pool is presented in three different orientations. As the melt pool is continuously moving, a teardrop shape forms, similar to what has been observed in welding. It has been demonstrated that the shape and size of the melt pool determine the type and number of defects but also the microstructure formed in the produced parts [23–25]. The distance between adjacent scan vectors is known as the hatch distance, as shown in **Figure 5c**. To ensure a fully consolidated part without significant defects or a lack of fusion, hatch overlap (**Figure 5c**) and re-melting of previously solidified layers are required to ensure a fully consolidated part.The process parameters are therefore set to penetrate a distance equal to 3–5 layers into already solidified material. This is schematically presented in **Figure 5b,** in which a color gradient illustrates the melt pool. An important consideration is that the layer just below the last re-melted layer exhibits a temperature close to the melting temperature. As new powder layers are melted, the distance from the melt pool increases, which gradually reduces the temperature. Therefore, as the process continues, an in-situ heat treatment in the build part is performed, which activates diffusion processes that lead to grain growth, phase transformations and precipitation [26–30]; this is further elaborated upon in Chapter 4. In addition, it has been observed that the rapid heating and cooling (due to the small interaction volume) followed by re-melting creates high internal stresses (by the constraining surrounding material).

When the entire cross-section has been melted, the build plate is lowered (according to the layer thickness). The layer thickness may be adjusted to compensate for any shrinkage generated during the solidification

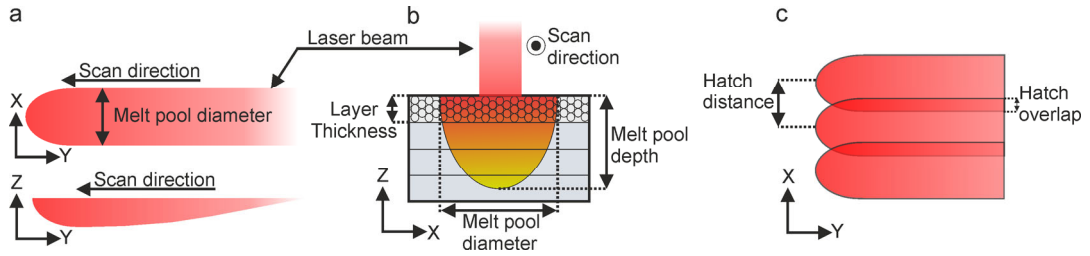


*Figure 5: Schematic overview of the most common process parameters.*

The path of the scan vector is defined by a scan strategy, which is essential for the final quality (e.g., defect types and number, microstructure, surface roughness and residual stresses) [31–35]. Various types of scan strategies exist, the most straightforward of which is unidirectional scanning, in which the scan vectors go from one side to another with the same direction in all layers, as illustrated in **Figure 6a**. This type of strategy is rarely used, as it has been demonstrated to significantly increase the residual stresses [36]. A faster version is bidirectional scanning (similar to meander scanning), in which the scan vectors turn back when reaching the part edge, as displayed in **Figure 6b**. Another common scan strategy is the chess strategy (or island scanning), illustrated in **Figure 6c**. The strategy divides the cross-section into smaller boxes in which, within the box, unidirectional or bidirectional scanning is used. The scan pattern is rotated within each box to reduce the residual stresses [37]. Furthermore,

there is the stripe strategy, which covers the cross-sections with stripes of a specific stripe width, as displayed in **Figure 6d**. Inside each stripe, a bidirectional pattern is used. When the stripe reaches the part edge, the stripe direction is turned by 180°.

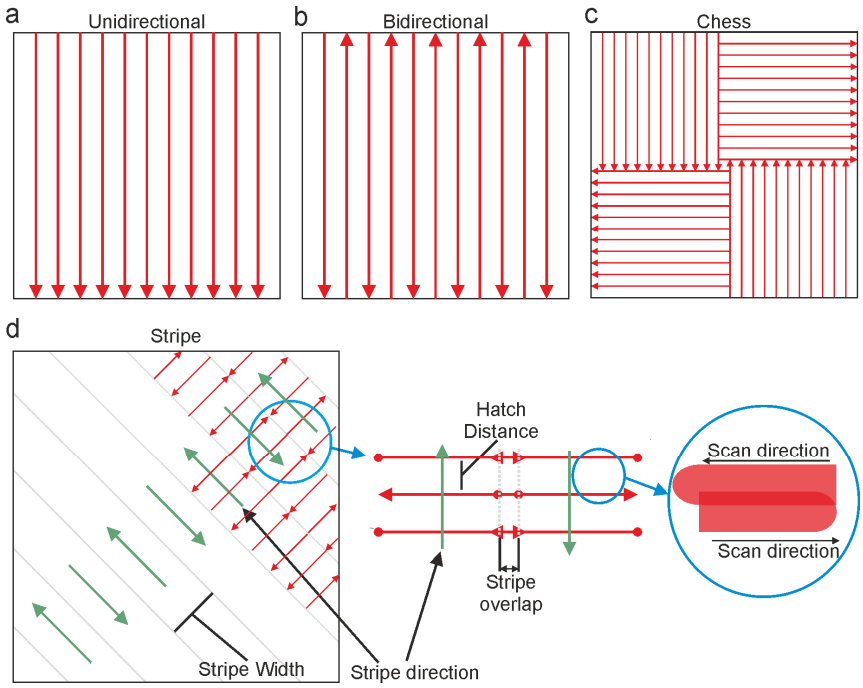


*Figure 6: Schematic overview of different scan strategies.*

The scan strategies are often combined with a rotation of the pattern as shown in **Figure 7**. Thus, the scan vectors or stripe orientations are rotated at a certain angle after each layer; this rotation is known as scan rotation. A scan rotation angle of 67° is typically used, as it achieves the optimal spacing between angles; that is, the orientation of the pattern has the maximum number of layers before the same orientation occurs again, as explained in detail by J.A. Pakkanen [38]. It should be noted that other rotation angles would generate similar spacings (i.e., 61°); however, most of the commercially available L-PBF processes use a 67° rotation angle as the standard. The scan rotation has demonstrated to be useful in reducing the residual stresses, which in turn reduce the risk of distortions [37,39].

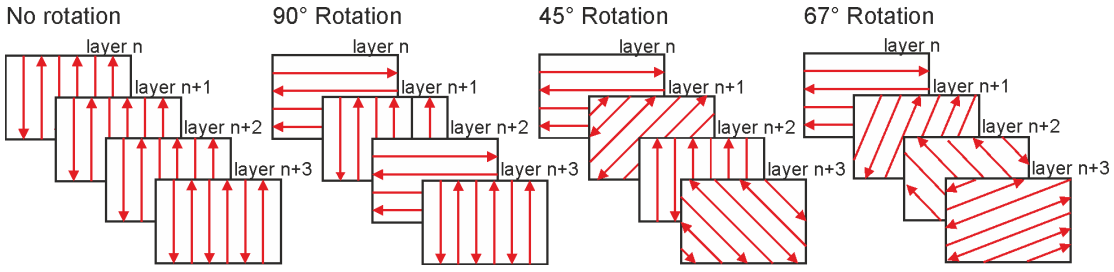


*Figure 7: Rotation of a bidirectional scanning pattern.*

When the entire cross-section has been melted, the outline/edge of the part is re-melted with a so-called contour scan, as illustrated in **Figure 8a**. Contour scanning is performed to improve the surface quality, as displayed in **Figure 8b and c.** Such surface smoothing has already been demonstrated for Inconel 625 parts by Koutiri et al. [40]. Contouring provides a re-melting of the part outline and is performed before or after the bulk cross-section area has been built.

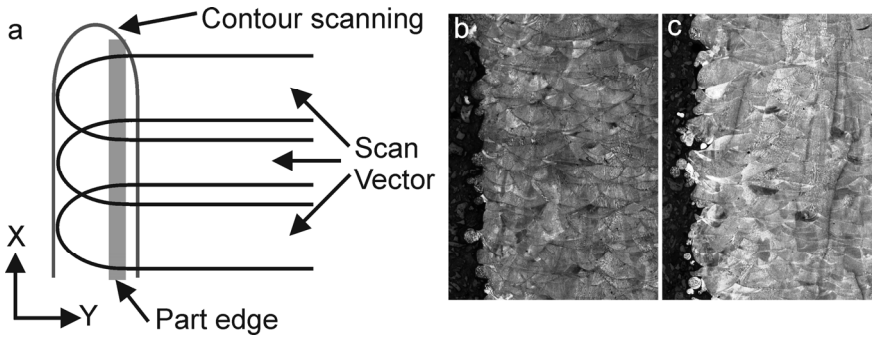


*Figure 8: (a) schematic overview of contour scanning, (b) optical micrographs of a sample produced with contour scanning and (c) an LOM image of samples produced without contour scanning.*

The protective atmosphere used in L-PBF is necessary to reduce the risk of oxidation of both the surrounding powder and the produced parts and to remove process by-products, such as spatter and fumes. It has been demonstrated that oxidation could lead to detrimental defects and compromise the powder recyclability [41,42]. By flushing a gas into the process chamber, oxygen and other impurities, such as nitrogen, can be diluted and hence prevent a diffusion-controlled reaction, such as oxidation or nitridation. The standard gas used for many of the L-PBF processes is argon, whereas nitrogen can be used for materials that are not sensitive to nitrogen dissolution and nitride formation at the rapid cooling rate encountered in additive manufacturing. This includes steels such as 316L, maraging and precipitation-hardening steels [43]. Pauzon et al. [44] indicated that using nitrogen in comparison with argon affected neither the microstructure nor the mechanical properties of 316L. Another function of the gas is the removal of the by-products generated during the melting process (e.g., projections, fumes and sputter, among others) by adding a flow of gas over the entire powder bed.

## 3.3 Economics and productivity of L-PBF

As indicated in the previous sections, one of the main challenges with additive manufacturing is finding meaningful applications that justify the use of a relatively expensive process. Therefore, a part produced with additive manufacturing must have increased performance or include other required features. An excellent way to realize this is to add complexity. It is, however, vital that the increased complexity translates into increased part performance. Yet, for many sectors, the costs are still too high (or the increased part performance is not justified compared with the cost) to motivate the implementation of additive manufacturing. Therefore, it is essential to increase the productivity to make the process more economically feasible. Some of the main factors that could be addressed to increase productivity and reduce costs are summarized below:

- Optimize process parameters for faster build speed
- Optimize build orientation
- Remove unnecessary material
- Use a cheaper powder
- Increase part performance
- Consolidate several parts
- Use a full build volume
- Consider post-processing and support structure

## 3.4 Design for laser powder bed fusion

The buildability is a critical aspect of additive manufacturing and refers to the ability to create the desired shape and could, to an extent, be maintained by applying specific design rules. Failing to properly design components for additive manufacturing creates a significant risk of producing components that either underperform and/or have deprived economic feasibility. Furthermore, improper design, orientation or placement of support structures can significantly increase the risk of build failure.

The design parameters depend on many factors (e.g., hardware and material), and it is difficult to provide generic guidelines. On the other hand, the success rate significantly increases if the engineers and designers have strong knowledge about the possibilities and limitations regarding additive manufacturing. Therefore, instead of providing specific values, this chapter presents some of the considerations that should be addressed. More detailed insight into design for additive manufacturing can be found in the book by Diegel et al. [17].

Additive manufacturing is frequently considered for an existing component, which likely can be produced faster and cheaper using a conventional method. The first step should consequently be to analyze the function and determine how the part complexity could be increased to improve the performance. The aim of re-designing a part for additive manufacturing should be to add more functions and features to maximize the part performance. The design should reduce the amount of material, which decreases both the build time and material cost. Adding other features, such as cosmetic details, logos, part numbers and assembly instructions, should be considered, as doing so does not add extra costs during manufacturing.

The build orientation should be considered from the beginning of the design process, as it influences the build speed, properties and need for supports. Considering these factors from the start could significantly reduce the required build time. In addition, the build orientation could affect the buildability of certain features, such as round holes. For example, large holes require support structures if they are oriented perpendicular to the build directions, as presented in **Figure 9a**, whereas no support structures are required if oriented parallel to the building direction, as illustrated in **Figure 9b**. The same can be said for overhangs, in which support structures might be necessary if exceeding the recommended value (often 45°), as presented in **Figure 9c**. If support structures are still required, the part design should be optimized so that the supports can be easily accessible. Furthermore, overhangs are often associated with a rougher surface [45]. Surfaces that require enhanced quality should therefore be orientated upward, as in **Figure 9d.**

The designer should also consider whether parts could be consolidated, as this increases the value by reducing assembly and tolerance costs. The final consideration is to ensure that un-melted powder within the part can be removed, which is especially important for small internal channels.

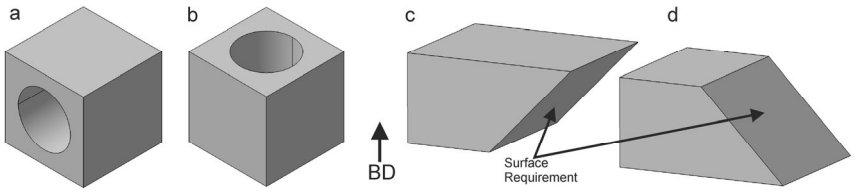


*Figure 9: Effect of different build orientations on a hole (a,b) and an overhang (c,d).*

# CHAPTER 4

# MICROSTRUCTURE

## 4.1 Stainless steel 316L

Stainless steel 316L is a widely used engineering material given its attractive combination of excellent corrosion resistance and good mechanical properties. The alloy is suitable for a wide range of sectors, such as gas and oil, chemical and petrochemical, marine engineering, food preparation, pharmaceutical and medical parts.

The alloy contains a high amount of chromium and nickel, which stabilizes the austenite phase up to the melting temperature, while the low amount of carbon reduces the risk of chromium-rich carbide formation, which is essential for maintaining excellent corrosion resistance.

As illustrated in **Figure 10**, processing 316L with L-PBF generates a fully austenitic microstructure with essentially no other phases. The fully austenitic microstructure of as-built samples has been confirmed by numerous studies [46–48].

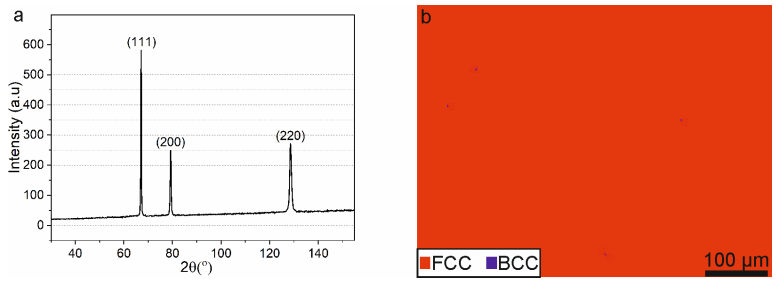


*Figure 10: (a) XRD pattern of as-built 316L samples showing only three austinite peaks. (b) a phase map obtained with EBSD showing the austenitic phase in as-built samples.*

## 4.2 Microstructure development

It was demonstrated that the thermal conductivity is approximately 100 times higher in solid material compared with the surrounding powder [49]. The heat generated from the melting process is therefore mainly dissipating by conduction through the already-solidified material toward the build plate. This heat flow is vital for the microstructure development of samples produced with L-PBF [50].

The rapid melting process and high cooling rates, together with the strong directed heat flow, produce a hierarchical microstructure with features that span from millimeters to nanometers, that is, large elongated grains separated by high-angle grain boundaries (HAGB), melt pool boundaries (MPB), cells and precipitates [2,30,51]. **Figure 11** presents an overview of the different features together with a size scale.

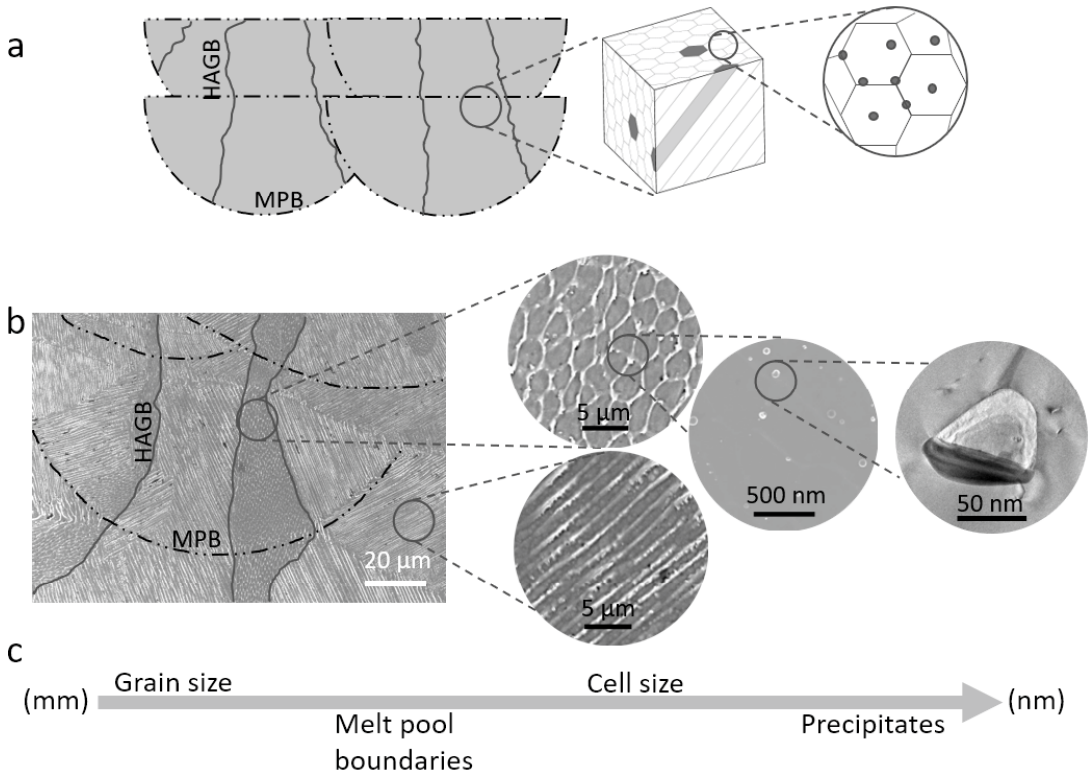


*Figure 11: Representative microstructure features of L-PBF processed 316L stainless steel presenting (a) a schematic overview, (b) SEM micrographs of the main features and (c) a length scale with the different features.*

The heat flow can be separated into a global and local heat flow, in which the global heat flow is the flow through the entire part, whereas the local heat flow is associated with the solidification of an individual melt pool. The melt pool begins to solidify from the melt pool boundaries toward the center, creating a local temperature gradient normal to the melt pool boundary. The global heat flow is created by the continuous re-melting of the layers, which forms a large temperature gradient along the building direction.

**Figure 12** presents a light optical micrograph of a cross-section of a 316L sample processed with L-PBF. The cross-section has been etched with oxalic acid after polishing. Two main characteristics can be assessed from the light optical micrographs. First, numerous melt pool boundaries can be distinguished, identified as half spheres along the cross-section. Second, irregularly shaped grains are elongated in the building direction. It can be seen that the grains grow epitaxially over several melt pool boundaries. The direction of the global temperature gradient is strongly affected by the movement of the laser beam, which is the main cause for the complex grain shape.

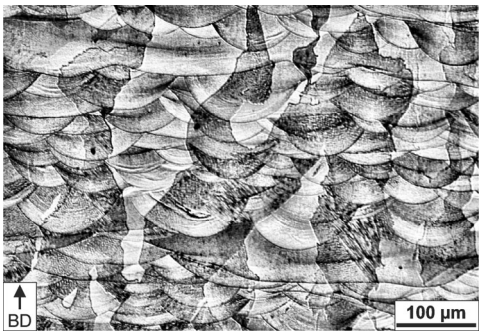


*Figure 12: Light optical micrograph of the cross-section in the building direction of an as-built L-PBF produced part*

Inside the columnar grains, a fine cellular structure appears, as illustrated in **Figure 13a–c**. These cells grow along the local temperature gradient (i.e., normal to the melt pool boundary), and as with the large grains, the orientation of the cells is strongly affected by the movement of the laser beam, yet also by the re-melting [30,46,48,52–54]. As observable in **Figure 13c,** the cell orientation might differ within the same melt pool, but cells can also continue to grow across melt pool boundaries. The size of the cells is generally between 0.5–1.0 µm in diameter with lengths reaching to more than 100 µm. The cell boundaries are known to have increased molybdenum content. Since the Mo atom is larger than the Fe atom, a local stress/strain field in the cell boundary is created, which increases the number of dislocations [2,48].

The cell formation is determined by the temperature gradient (G) and growth rate (R) at the solidification interface, where the product (i.e., G*R) represents the cooling rate [26,50,52]. The solidification mode may change from planar to cellular, cellular-dendritic or dendritic depending on the undercooling [50,52], as schematically illustrated in **Figure 13d**. The solidification mode is also determined by the ratio between the temperature gradient and growth rate (i.e., G/R). A high G/R ratio generates a planar solidification, while a low G/R generates a dendritic solidification. The cellular structures observed in L-PBF indicate an intermediate G/R. Furthermore, the cooling rate given by the product G*R controls the size of the cells.

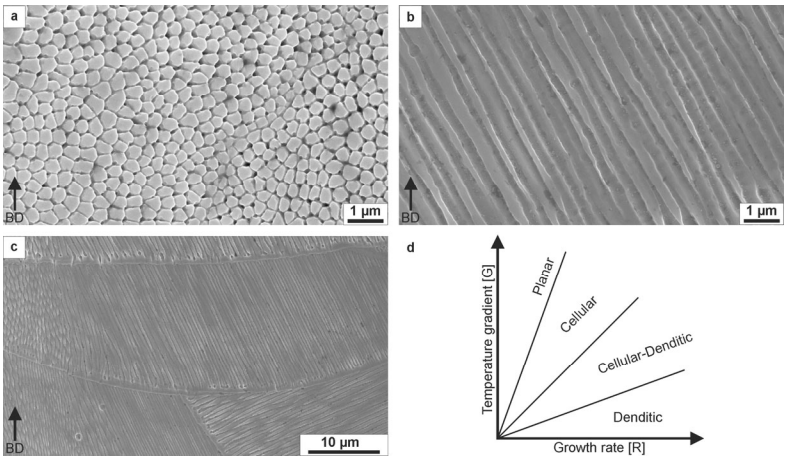


*Figure 13: SEM micrographs displaying a fine sub-cell structure in two different orientations, (a) perpendicular to the building direction,(b) parallel to the building direction and (c) different cell orientations within the same melt pool. (d) schematic overview of the effect of the temperature gradient and growth rate on the different solidification modes.*

Since high cooling rates, in the range of $10^4$ to $10^6$ K/min, have been reported, fine cellular morphology is formed [50,52]. The growth of the cellular structure is controlled by the advancement of the solidification front, which in turn is controlled by the thermal gradient. Higher heat transfer results in a finer cell structure, while the slower dissipation of heat results in a coarser cell structure [26,50,52]. Compared with microstructures produced by manufacturing techniques that traditionally have been considered to include rapid cooling, such as welding, the microstructure obtained in L-PBF is much finer and more unique compared with microstructures obtained by other metal-forming processes [53,54]. By changing the processing parameters, the alteration of cell sizes can be achieved, owing to the different thermal histories. Using higher thermal input leads to coarsening of the cells [8,50].

The orientation of the cells can be correlated to the texture of the sample, in which the cells that grow parallel to the building direction correspond to a <001> texture, as schematically illustrated in **Figure 14a** [24,25]. Thus, the shape and radius of the melt pool boundaries are significant for texture development, since the cells grow normal to the melt pool boundary. At the bottom of the melt pools, the cells grow parallel to the build direction, and as the melt pool boundary becomes steeper, the texture deviates more from <001> (i.e., becomes more random), as presented in **Figure 14b**. In other words, it becomes more difficult to maintain the easy-growth direction. At a certain point, the angle between the normal and building direction is approximately 45°, which means that a predominant <101> texture is formed, as displayed in **Figure 14c**. **Figure 14** is simplified, as a transition occurs with other orientations between <001> and <101>, such as <012>. In addition, Sun et al. [25] explained that at a certain angle of the melt pool boundaries, the epitaxial growth mechanism takes over, and the <101> orientation is preserved as the global temperature gradient takes over. Furthermore, the variety of crystallographic orientations, ranging from a strong <001> or <101> texture to a more random texture [24,31–33,46,51,55–57], can also be realized by using different process parameters and scanning strategies, as both the temperature gradient and melt pool shape are affected [54,58,59]. For example, increasing the energy density produces a stronger <101> texture, whereas low energy generates a more random texture [8,25].

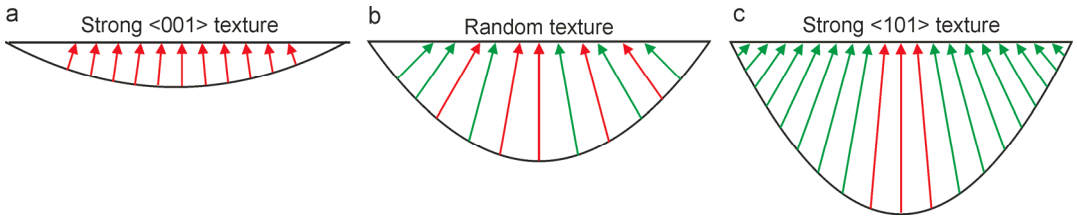


*Figure 14: Schematic image displaying the formation of different textures as a function of melt pool depth, where red arrows indicate <001> and green arrows indicate <101>.*

The EBSD orientation map in **Figure 15a** displays a strong <101> texture of 316L samples produced with an EOS M290 machine. Furthermore, as illustrated in **Figure 15b,** the microstructure at the edge of the same sample consists of smaller grains inclined toward the center of the sample. The small inclined grains have random crystallographic orientations. This type of microstructure has been observed for other materials as well, such as Ti-6Al-4V that has been processed by additive manufacturing [60].

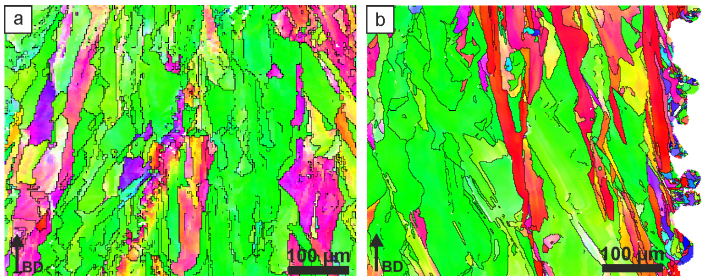


*Figure 15: EBSD orientation map of 316L samples produced with an L-PBF process obtained in (a) the center of the samples and (b) at the part edge.*

The microstructure development in L-PBF is similar to the microstructural development that occurs during the solidification of cast ingots, in which finer grains are formed in the chill zone close to the cast mold [61]. As the solidification progresses, columnar grains begin to form that grow toward the center of the ingot. In the end, the center of the ingot forms an equiaxed grain structure. In the case of L-PBF, the powder bed surrounding the part (mix of powder and gas) acts similar to the cast mold. Then, many stable nuclei are created close to the component/powder interface. The metal particles that are only partially melted act as the nucleation sites for creating smaller inclined grains. The adjacent powder extracts some of the latent heat, even if most of the heat is extracted through the part, hence changing the direction of the heat transfer and thereby the thermal gradient and finally the cell growth direction. However, in contrast with casting, heat is sequentially added, which creates a heat flow in the direction normal to the building direction through the build plate. This creates a strong thermal gradient along the sample. Therefore, the grains at the edge begin to grow upward and inward, and in the center of the sample, large elongated grains are formed. The grains in the center of the part continue to grow epitaxially. The columnar grain growth continues, and no transition to the larger equiaxed grains occurs as long as more heat is added.

Heat treatments of L-PBF parts are generally conducted to reduce the possible residual stresses caused by the rapid cooling cycles in combination with the constraints connected to the anchoring of the part on the build plate. The conventional low-temperature stress relief treatment commonly applied to cold-worked 316L stainless steel can be performed. This consists of heating at a temperature between 160°C and 415°C followed by slow cooling, and it allows for reducing stresses without impacting corrosion or mechanical properties [62]. This type of heat treatment is typically recommended by the L-PBF machine manufacturers [63]. One might also consider a traditional high-temperature annealing heat treatment (between 900°C and 1100°C), followed by sufficiently rapid cooling to avoid the formation of grain boundary carbides. This would also mean to avoid, for instance, the sigma phase, the formation of which is much slower. A balance between temperature and cooling rate may be crucial, as quenching is likely to reintroduce stresses with an increased risk of stress corrosion. Hence, heat treating stainless steel at higher temperatures is a compromise between sensitizing the material to grain boundary corrosion and stress corrosion.

# CHAPTER 5

# MECHANICAL PROPERTIES

## 5.1 Strengthening mechanisms

Plastic deformation is the generation, movement and accumulation of dislocations produced by applying a physical or thermal stress surpassing a critical stress for yielding. The applied stress acts to move dislocations, and the strength of the material is given by the ability to hinder the movement of these dislocations. The movement is hindered by internal obstacles, such as other dislocations, internal interfaces, grain boundaries and secondary phases. There exist different methods for creating these obstacles, known as strengthening mechanisms, namely solid solution strengthening, work hardening, grain refinement and precipitation hardening. Most materials are strengthened by a combination of these mechanisms.

Many steels can also be strengthened via transformation hardening. However, in the case of 316L, transformation hardening is not viable because martensite does not form, due to the low carbon content, and the deformation-induced formation of martensite is less prone for 316L than what is frequently observed for stainless steel 304L. Furthermore, precipitation hardening is not recommended, since it negatively affects the corrosion resistance. However, 316L is often strengthened by work hardening (also known as dislocation hardening) via cold rolling or forging, which results in a significant increase of dislocations. Work hardening increases the strength but reduces the ductility, recognized as the strength-ductility trade-off.

## 5.2 Deformation by twinning

Two prominent mechanisms exist for plastic deformation: slipping and twinning. These two mechanisms compete with each other, and a material may undergo both mechanisms at different stages of the deformation cycle depending on its fundamental properties, even if slipping is far more common. The deformation twinning causes changes in the plane orientation so that further slip can occur, creating a twin boundary. The twin boundaries maintain low energy compared with the high-angle grain boundaries; thus, they can store dislocations more efficiently, which, for example, is good for work hardening properties [2,51]. In addition, dislocation can pass through or glide along the twin boundaries, and in this way, the dislocation enhances both the strength and ductility [64].

Deformation by twinning requires low stacking fault energy and dislocation pile-ups. However, stainless steel 316L has a stacking fault energy considered to be in the medium range of approximately 20 $mJ/m^2$ [24,65]. Thus, twinning is not that common in 316L. However, some factors exist that promote deformation by twinning in L-PBF produced samples. First, the nitrogen content in the produced parts tends to be higher compared with traditionally

manufactured parts; this originates from the nitrogen used during the powder manufacturing [66]. The increased nitrogen content then reduces the stacking fault energy [67]. The fine cellular structure with high dislocation density promotes dislocation pinning [2,46]. In addition, Sun et al. [24] and Sinha et al. [68] demonstrated that <101> oriented grains are more favorable for twinning compared with <100> oriented grains. As observed, the L-PBF produced sample is often exhibiting a strong <101> texture. Therefore, the primary cause of increased twinning in L-PBF produced samples can partially be associated with a nitrogen pickup, increased dislocation pinning and a strong <101> texture.

## 5.3 Size effect

The size effect is a phenomenon that specifies that the mechanical properties are affected by the sample size and grain size. The phenomenon arises when the ratio of the sample thickness to the grain size (t/d) is less than a certain value [69–71].

The principle is that grains can be either favorably oriented or unfavorably oriented with respect to the loading direction. The weakest link is consequently created when several unfavorably oriented grains are connected along the full thickness of the sample, similar to the weakest link of a chain [69,72]. This is schematically illustrated in **Figure 16**, in which the dark gray color indicates unfavorably oriented grains. Thus, a reduced number of the load bearing grains would result in an anisotropic deformation behavior, as few grains would determine the load-bearing capacity [69,73,74]. As the thickness increases, the probability of having the weakest link significantly decreases [69,75]. The sample strength becomes randomly and evenly distributed over several grains, creating an isotropic deformation behavior.

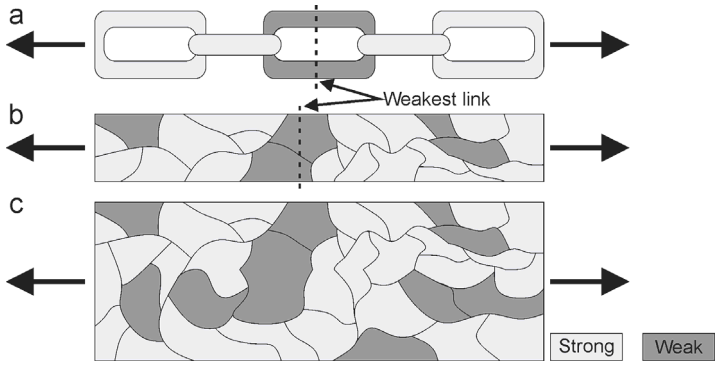


*Figure 16: Schematic image presenting the weakest link concept of (a) the chain, (b) thin sample and (c) thick sample. Redrawn from* [69].

Related to the sample size, this is an effect recognized as the slimness effect or slimness ratio and is a geometrical consideration [76]. It has been experimentally revealed that the average elongation to fracture is reduced when the length over square root of the cross-sectional area ratio, $(\frac{L_0}{\sqrt{A_0}})$, is reduced.

## 5.4 Properties of L-PBF produced parts

Laser powder bed fusion produced 316L exhibits improved yield strength (YS) but similar or slightly lower ductility compared with samples produced via other processes, such as cold rolling or casting [29,48,50,53,77–79]. When processing 316L using conventional methods, a low YS is obtained but with a strong work hardening ability. The strong work hardening ability

generates a relativity high ultimate tensile strength (UTS), as illustrated by the black curve in **Figure 17a** and in the bar diagram of **Figure 17b**. However, L-PBF produced samples exhibit both high YS and UTS yet have a low work hardening ability, resulting in roughly the same UTS value as the cold rolled sample. As-built L-PBF produced components should consequently be designed with a higher safety margin, as they possess a lower YS/UTS ratio compared with components that have been processed using conventional methods.

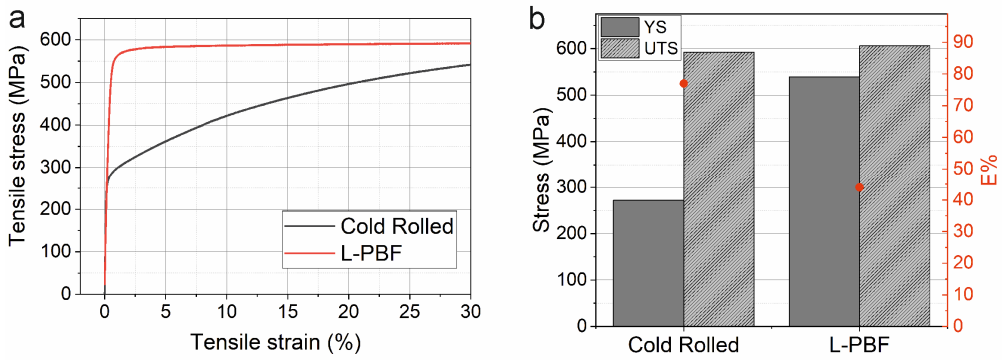


*Figure 17: Tensile properties of cold-rolled and L-PBF produced the sample: (a) tensile test curve and (b) summary of YS, UTS and ductility. The UTS and the ductility value is not visible in the tensile test curves due to the limited length of the extensometer.*

The tensile properties of L-PBF produced 316L are affected by several factors. For example, the dislocation movements are hindered by other dislocations [52,80], grain boundaries [80], cells [30,50], nano-sized inclusions [81] and segregations [30]. The cells are considered the most significant feature for the tensile properties, and a linear dependency exists between decreasing cell size and increased tensile properties [2,51].

The cells accumulate the dislocations, which generate a positive effect on the tensile strength [2,30,80]. In addition, the cells are relativity stable during the deformation and remain unchanged in shape and size at lower strain [2]. This allows the dislocation movement to be hindered over a longer period, which contributes to lower and more steady work hardening, thus improving the ductility [2,46,82]. At higher deformation, the cells begin to elongate, increasing dislocation pile-up, which promotes deformation by twinning. The dislocation twinning further helps to sustain the steady strain hardening at high deformation, which further improves the ductility while maintaining high strength [2,68,80].

# CHAPTER 6

## EXPERIMENTAL PROCEDURES

In this chapter, a general overview of the feedstock material, sample design and process parameters is provided. The characterization tools and settings are explained with a brief discussion about the implications of some of the approaches.

### 6.1 Sample manufacturing

The samples provided in this study have been fabricated with gas atomized stainless steel 316L powder supplied by Höganäs AB. The powder had a particle size distribution of 25–53 µm. The samples were produced with an EOS M290 machine (Electro Optical Systems GmbH, Germany) equipped with an Yb-fibre laser with a maximum nominal power of 400 W and a chamber with a maximum build height of 325 mm with a 250 mm x 250 mm build area. The EOS M290 machine is fully developed for commercial use and is provided with sets of parameters for a variety of materials, including 316L. The builds were conducted in an argon environment, where the oxygen content was maintained below 0.1%. The samples in Papers I, II and III were fabricated with standard process parameters (version 1.10) with the pre-defined stripe scanning strategy (as described in Section 3.2). In Paper III, the effect of the process gas was investigated, and builds were conducted in argon, nitrogen and helium; these samples were produced without contour scanning. Paper IV investigated the effect of scan speed (800–1400 mm/s) and hatch distance (0.06–0.12 mm), while all other parameters were kept according to standard process parameters. The combination of these process parameters was evaluated by the volumetric energy density (frequently abbreviated as energy density), given from the equation $E = \frac{P}{v*h*l}$ , where E is the total volumetric energy density (J/mm$^3$), P is the laser power (W), v is the scan speed (mm/s), h is the hatch distance (mm) and l is the layer thickness (mm). Paper V investigated the effect of scanning strategy on samples produced using a bidirectional scanning with different scan rotations. The samples in Papers I–V were built with a layer thickness of 20 µm, while the samples discussed in Paper VI were produced with a layer thickness of both 20µm and 80 µm. No predefined process parameters were available for the 80 µm layer thickness; new process parameters were therefore developed based on the evaluation of 41 cubes with a wide range of process parameters. The final process parameters were selected based on porosity, process stability, build time and tensile properties. The selected process parameters used for performing a deeper investigation are presented in **Table 2**.

*Table 2: Selected process parameters.*

| Power | Layer Thickness | Scan Speed | Hatch Distance | Stripe Width |
|---|---|---|---|---|
| 295 W | 0.08 mm | 800 mm/s | 0.12 mm | 10 mm |

Since the approaches for the appended papers varied, different sample designs were needed. **Figure 18** presents schematic drawings and dimensions of the produced samples. The main reason for using the design in **Figure 18c** instead of the standard bar in **Figure 18d** is because the alternative tensile test samples can be fabricated faster, allowing for more samples to be tested

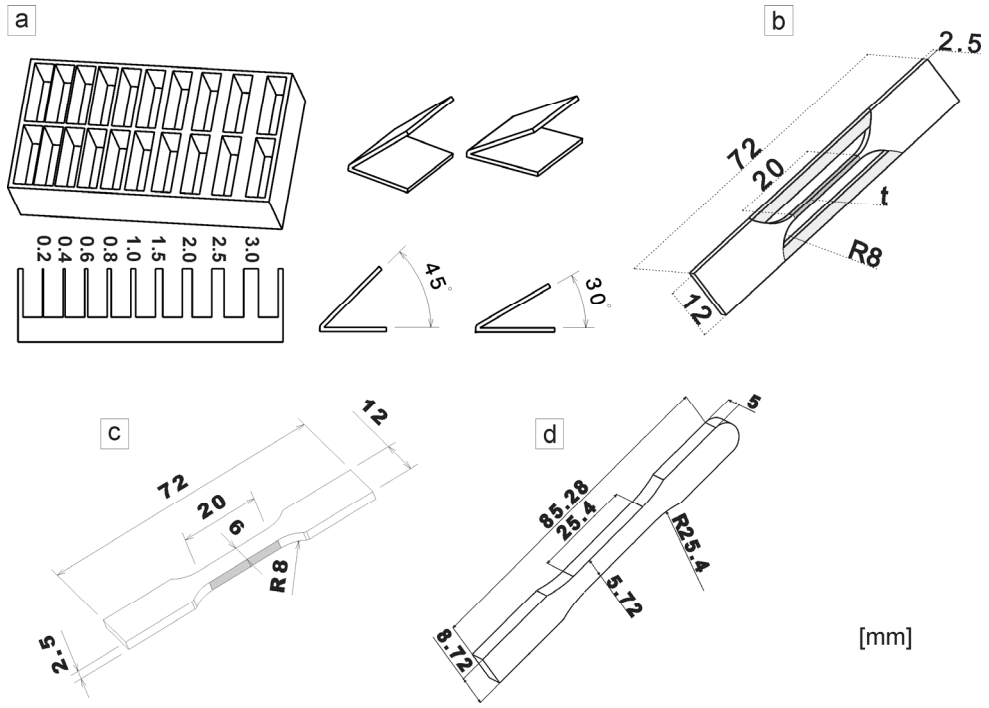


*Figure 18: A schematic overview of the isometric and cross-sectional views of (a) straight ribs and inclined ribs used in Paper I, (b) tensile test bar with varying gauge length thickness (t) used in Papers II and III, (c) tensile test bar used in Papers IV and V and (d) standard tensile test bar with dimension according to ASTM E8/E8M−16a used in Paper VI.*

## 6.2 Sample preparation

The samples used for microstructure characterization were prepared via standard metallographic procedures. The cross-sections were mounted in conductive resin and subsequently ground and polished according to Struers standard procedures for preparing stainless steel. Hence, they were ground in steps with SiC paper and polished with 3 µm suspension. The final polishing was performed with 0.04 µm standard colloidal silica suspension (OP-S) for about 12 min (the last 2 min with water). A force of 25 N/sample was applied for both the grinding and polishing. Subsequently, the samples used for microstructure characterization were electrochemically etched in 10 vol. % oxalic acid using a platinum electrode as the counter cathode, with a potential of 3 V. It was discovered that the oxalic acid preferentially attacks the cell boundaries. In Paper V, the cell size was of interest, and the samples were therefore chemically etched using Glyceregia (10 ml $HNO_3$, 20 ml HCl, 30 ml glycerol) to reveal the cell boundaries. The differences between the etching methods can be observed by comparing **Figure 19a and b.** When etching with oxalic acid (**Figure 19a**), the cell boundaries are preferentially etched, whereas Glyceregia etches the cell interior. The cell boundaries appear brighter in the provided SEM image. This observed difference could potentially be used as an indication of the elements that are segregated at the cell boundaries; however, this issue was not investigated further.

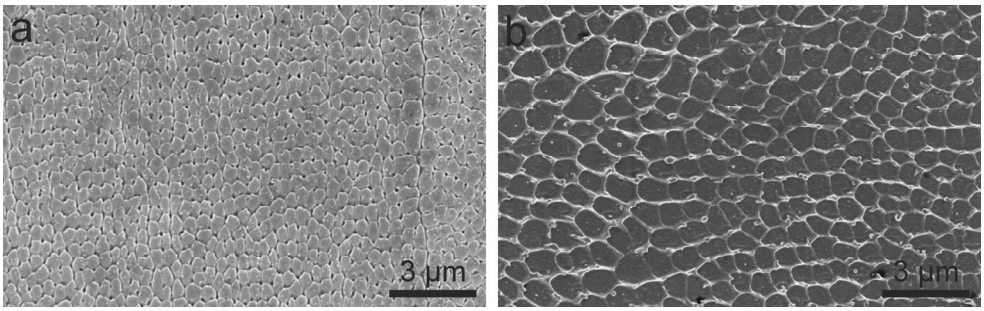


*Figure 19: SEM image presenting the difference between the two etching methods: (a) oxalic acid and (b) Glyceregia.*

All samples were analyzed in as-built conditions after being removed from the build plate with a band saw. The coordinate system used in this thesis for the cross-sections is presented in **Figure 20.**

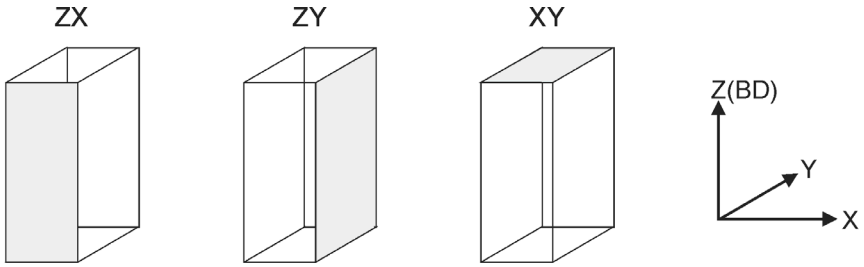


*Figure 20: Planar cross-section of the prepared samples.*

## 6.3 Characterization tools

### 6.3.1 Light Optical Microscopy (LOM)

Light optical microscopes of type Leitz DMRX and ZEISS Axioscope 7 were used for the microstructure characterization and porosity determination. The porosity was obtained via a thresholding procedure of several micrographs of each sample using ImageJ (an image processing software commonly used for this type of measurement [83]). The thresholding procedure was conducted by dividing the image into two components (black and white) based on a cut-off value in pixel contrast (binary image). However, as can be seen in **Figure 21a**, the pores do not have well-defined edges, so it is difficult to determine when a pixel should be considered bulk or pore. The thresholding operation is then used to determine when an edge pixel should be considered black or white. This method appears to be the most accurate procedure for determining small density variations of high-density parts. However, as shown in **Figure 21b and c,** depending on where this threshold is set, the evaluated density varies. For example, at the arrow in **Figure 21a,** a barely visible pore is indicated that is not visible in **Figure 21b,** while in **Figure 21c,** the cut-off value was set to be higher, and the pore is visible. The different cut-off values generated a difference in the porosity of approximately 0.25%. It can be assumed that by carefully obtaining the micrographs (good focus) and properly applying the threshold operation, an accurate value can be generated. However, a slight difference in depth of focus (as would be the case when using, for example, a stitching operation) might cause a substantial variation. In this thesis, over 25 images on different cross-sections were obtained to determine the porosity. However, due to the uncertainties mentioned above, most of the density values are reported to only one decimal. In this context, smaller changes are of minor importance for the measured properties. Furthermore, it is important to note that

inclusions and porosities cannot be distinguished, and hence, inclusions are potentially counted as pores in this study. It should be noted that **Figure 21** was used to emphasize the problem (a better focus could be achieved).

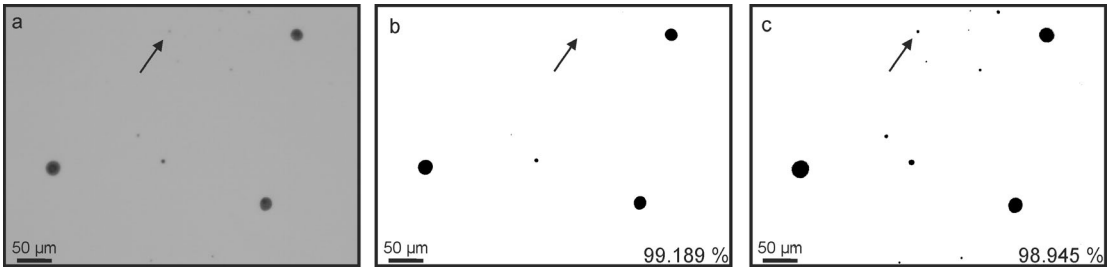


*Figure 21: Effect of threshold operations on the density. (a) a light optical image displaying pores, (b) low cut-off value and (c) high cut-off value. The arrows indicate a pore that is removed by a combination of the threshold operation and focus depth.*

### 6.3.2 Scanning Electron Microscopy (SEM)

Scanning electron microscopy (SEM) provides information about microstructural features with a high spatial resolution, even at higher magnifications. By directing an electron beam through electromagnetic lenses onto a sample surface, different types of radiation are generated, such as secondary electrons, backscatter electrons and X-rays. The emitted radiation can be used to obtain information about the sample. In this study, microstructural features of samples were investigated using SE imaging in a LEO Gemini 1550 (LEO GmbH, Oberkochen, Germany) scanning electron microscope.

Investigation via the electron backscattered diffraction (EBSD) technique was performed with a Nordlys II detector (Oxford Instruments). For the measurements, an acceleration voltage of 20 keV and a working distance of 10–20 mm were used. The chosen step size was between 0.05–3.0 µm. The EBSD maps were acquired with AZtecHKL software and processed using Channel 5 software. The grain boundaries were defined to have a crystallographic misorientation of > 10°. All EBSD orientation maps are presented in inverse pole figure coloring using the common color coding, as illustrated in **Figure 22.**

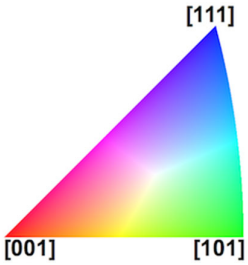


*Figure 22: Standard inverse pole figure color code.*

Electron backscattered diffraction is a powerful tool for obtaining crystallographic information from crystalline materials. In this thesis, the EBSD technique was used to investigate the texture, grain characteristics (orientation, size and shape), phase composition and local plastic strain. The analyzed area was small compared with the part sizes. Therefore, it was essential to obtain several maps for each sample. The EBSD technique can also be used for analyzing plastic strain by determining the local misorientation of the crystallographic lattice (i.e., lattice distortion). The average misorientation can then be calculated by averaging the misorientation

between a center pixel (a kernel) and all its neighboring pixels. Afterward, the average values can be presented in something known as kernel average misorientation (KAM) maps. The KAM maps were calculated with the nearest neighbor pixels having a 2° misorientation threshold (to avoid the influence of grain boundaries). The KAM maps were used for qualitatively evaluating the dislocation density.

### 6.3.3 X-Ray Diffraction (XRD)

X-ray diffraction (XRD) can be used for identifying phases by investigating the crystal structure. By using Bragg's law [84], patterns of intensity peaks can be detected. These peaks are compared and identified using the database provided by the Joint Committee for Powder Diffraction Standard (JCPDS). In this thesis, a Bruker AXS D8 Advance instrument was used, which has a 2Θ range between 30° and 140°. The radiation source was CrKα ($\lambda = 2.29$ Å), and the acceleration voltage was set to 35 kV with a current of 40 mA. JPDF-Card 00-033-0397 was used for peak identification.

X-ray diffraction was used to determine whether there were any phase changes and to estimate the dislocation density. However, as emphasized by Pešička et al. [85], XRD line profile broadening methods (the method used to determine dislocation density with XRD) consider only the free dislocations (a minor portion of the total number of dislocations). However, the purpose was to indicate differences between samples, which is feasible with sufficient accuracy.

### 6.3.4 Mechanical testing

Tensile testing is one of the most used methods for evaluating the properties of metallic materials, primarily because it is simple, fast and relativity cheap and provides fundamental properties for the product development process.

All samples were tested at room temperature in their as-built condition. The tests were conducted with an Instron 5500R machine with a clip-on extensometer, and the experiments were strain rate controlled with a crosshead velocity of 0.025%/s. The dimensions of the samples were measured using a caliper. The reported results were obtained from three to five samples for each set.

The Vickers hardness was measured with a Struers DuraScan hardness tester with a 1 kg load. The reported hardness values represent the average from at least five indents.

# CHAPTER 7

## SUMMARY OF RESULTS AND DISCUSSION

This chapter summarizes the results and discussions from the appended papers with the addition of some complementary results, in which most of the arguments are framed around the appended papers. This chapter concludes by demonstrating how the results can be implemented to emphasize the implication of the presented research.

### 7.1 Baseline

As presented in Chapter 4, a large variety in microstructure has been reported for 316L samples produced with L-PBF. It is established that the microstructure is influenced by the process parameters, assuming also potential differences between different machine brands and models. A baseline is thus created, based on results obtained from standard dimension tensile test bars. **Figure 23** presents the microstructures (in ZX and XY) representative for 316L samples processed with an EOS M290 using standard process parameters for the material of interest. As illustrated in **Figure 23c**, the submicron-sized cellular structure is observed inside the melt pools, with differently oriented cells and a range of sizes. A more detailed description of the microstructure in its as-build state can be found in Section 4.2.

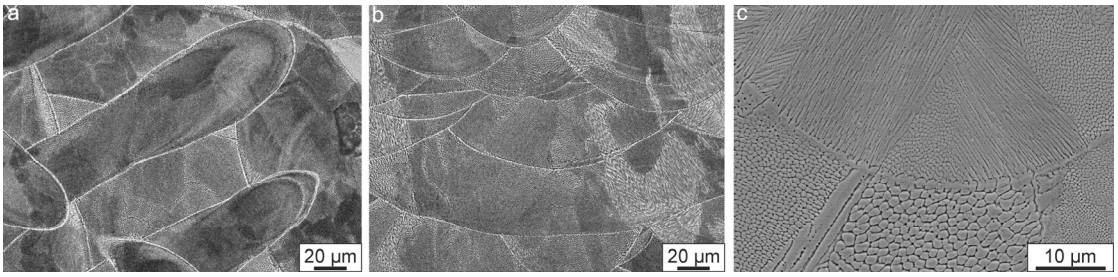


*Figure 23: Microstructure of a standard bar showing (a) XY-cross-section at low magnification (b) ZX-cross-section at low magnification and (c) ZX-cross-section at high magnification*

Electron backscattered diffraction orientation maps obtained from the ZX and XY cross-sections can be seen in **Figure 24a and b**. In both cross-sections, a strong <101> texture can be found. The ZX cross-section reveals large elongated grains, while the XY cross-section presents more equiaxed-shaped grains. The microstructure is exceptionally complicated, with a substantial variation in grain sizes created by the constant movement of the laser beam. For comparison, an EBSD orientation map was acquired from a conventional 316L sheet presented in **Figure 24c** and presents typically shaped grains with well-defined grain boundaries.

Parts were also produced at a 45° inclination to the build plate, but the inclination did not appear to influence the direction of the large elongated grains. However, a more random texture

compared with that in the vertically built samples was observed. The build angle changes the heat transfer direction, and thus the thermal gradient is changed, which reduces the texture (Paper I).

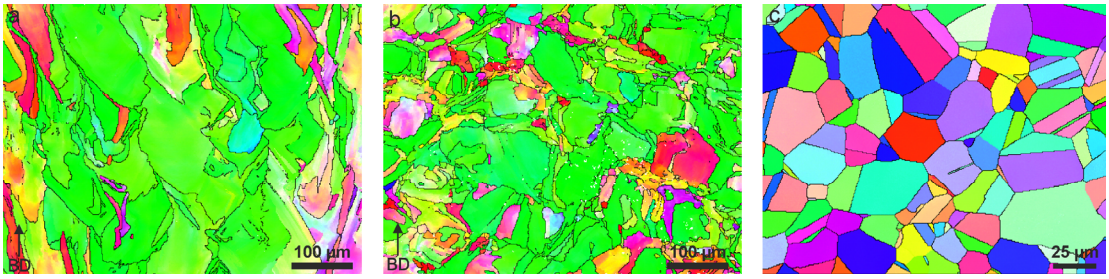


*Figure 24: EBSD orientation maps of cross-section samples (in building direction) from the center of the standard bar of the (a) ZX-cross-section, (b) XY-cross-section and (c) cross-section from the conventional sheet metal formed 316L.*

The tensile properties obtained from two build orientations are presented in **Figure 25**. It is evident that the build orientation affects the yield strength, ultimate tensile strength and elongation to fracture (ductility); this anisotropic behavior has been reported in numerous studies [53,55,86–88]. Most of the presented results in this thesis were obtained in the weakest direction (vertically built samples). Still, even the weakest direction exhibits static properties well above the ASTM 240/A240M−18 recommended values for cold-rolled stainless steel (indicated by the horizontal lines in **Figure 25**

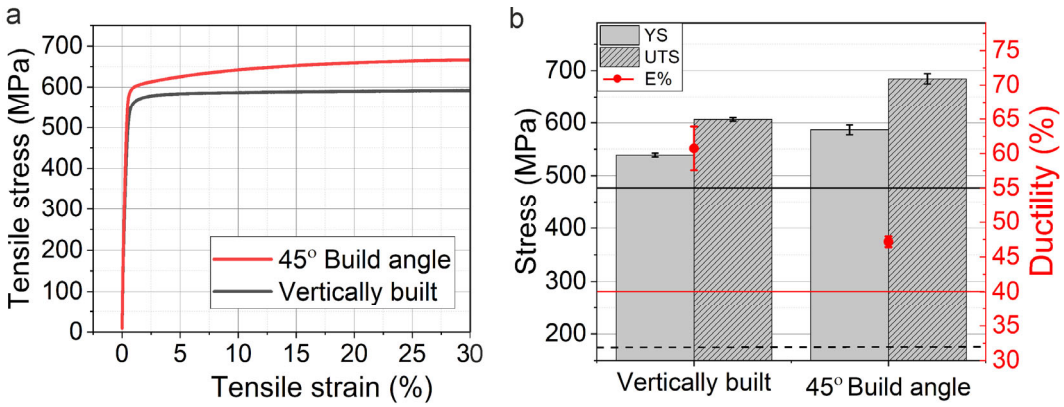


*Figure 25: Summary of the tensile properties: (a) representative tensile test curve and (b) tensile properties obtained from five individual tests. In (b), the solid black line represents the required values of UTS, the dashed line represents YS and the solid red line represents the ductility for cold-formed stainless steel 316L provided in ASTM 240/A240M−18.*

High-magnification SEM images and EBSD orientation maps of the samples in the as-built and heat-treated conditions are provided in **Figure 26**. Both the cellular structure and the melt pool boundaries are visible after heat treatment at 450°C. However, after heat treatment at 1000°C, the samples present neither a cellular structure inside the grains nor any melt pool boundaries. The high-angle grain boundaries appear to be unaffected by the heat treatment at 1000°C. The EBSD analysis further reveals that misorientation is still present inside the larger grains, which suggests that recrystallization has not occurred even after heat treatment at 1000°C for 2 h. The diffusion of the substitutional elements at 450°C is very low; therefore, as long as limited or no diffusion occurs, both the cells and the melt pool boundaries would remain intact, as expected for any low-temperature stress relief annealing. As the temperature is increased to

1000°C, diffusion becomes more significant, and the dislocations are reduced/annihilated. Hence, heat treatment at 1000°C results in the dissolution of the solidification structures, namely the melt pool boundaries and cells. The high-angle grain boundaries, on the other hand, appear to be stable at the annealing temperature of 1000°C. Even small grains (less than 10 µm) can still be observed after the high-temperature annealing treatment.

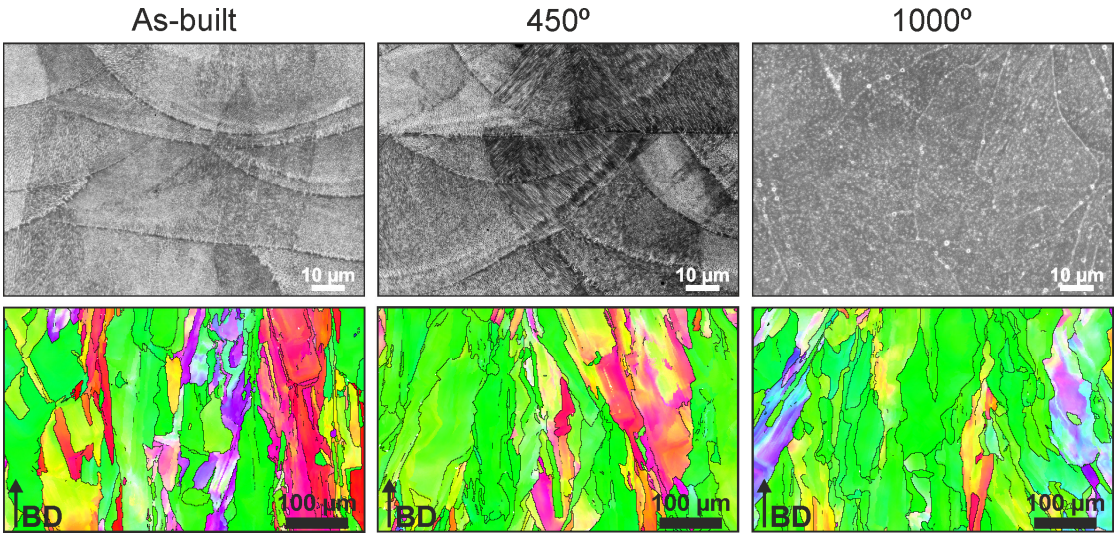


*Figure 26: SEM images and EBSD orientation maps of samples in as-built and heat treated at 450°C and 1000°C states with an upward building direction.*

It was then demonstrated that removing the cell substructure via high-temperature heat treatment reduces the yield strength and increases the work hardening ability. The samples then exhibit properties similar to the cold-rolled and annealed sample, as observable in **Figure 27**. This proves the importance of the contribution from cellular structure to the improved tensile properties of L-PBF produced samples.

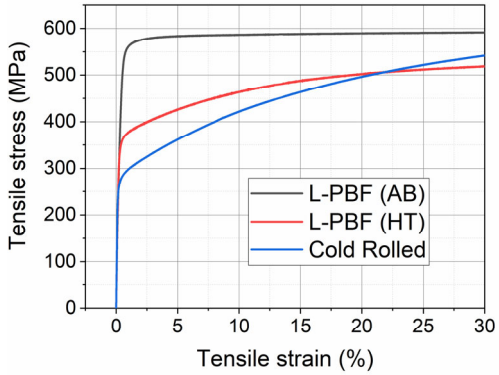


*Figure 27: Tensile test curve displaying the cold-rolled and annealed, as-built (AB) and heat-treated (HT) at 1000°C L-PBF samples.*

## 7.2 Effect of part design

To investigate the effect of part design on the microstructure and tensile strength, samples with different thicknesses and angles were fabricated using standard process parameters. The sample design and dimensions are presented in **Figure 18a and b**. A light optical analysis of the un-etched samples indicated that density is not affected by the part design or build orientation.

Buildability is an essential aspect for L-PBF and refers to the ability to fabricate the desired shape without compromising material properties or process stability. Buildability is strongly associated with the adaptation of the design guidelines and selecting suitable process parameters. However, neither the design guidelines nor the process parameters are typically not developed for fabricating lightweight structures. For example, the recommended constraint in the thickness-to-height ratio is 8:1, which occasionally must be exceeded. In Paper I, it was discovered that ribs with a 0.2 mm thickness with a building height of 20 mm (100:1 ratio) could be successfully fabricated. Furthermore, tensile bars with a thickness of 1 mm (20:1 ratio) were successfully built. However, attempts to fabricate tensile bars with thicknesses of less than 1 mm failed due to the fragility of the design. The origin of the failure was small vibrations created by the recoater blade, which eventually resulted in part collapse. Hence, application of the soft recoater can provide a solution to the issue observed. Another general recommendation is that a build angle of less than 45° should be supported. It was demonstrated that 1 mm ribs with a build angle of 30° were successfully built without support structures but with higher surface roughness and poor dimensional accuracy.

**Figure 28** presents EBSD orientation maps acquired in the center of the ribs with 1.0, 0.4 and 0.2 mm thicknesses. It can be seen that above a 1 mm thickness, a strong <101> texture is created similar to the standard tensile test bar (**Figure 24a**). A transition from this strong <101> texture to a more random texture was observed when the part thickness was reduced (**Figure 28b and c**)**.** The strong <101> texture appears to be formed when the heat flow is aligned with the building direction and a strong, uniform thermal gradient can be maintained. In other words, the reduction of component thickness changes the heat transfer rate and the direction. This can be further understood by considering the grains close to the part edge, where it was demonstrated that smaller grains had been formed (**Figure 28b and c**). The small grains grow inward toward the part center and were observed regardless of part thickness. The smaller grains were observed up to about 100 µm from the part edge, after which large elongated grains were detected. These small inclined grains more or less dominate samples with a thickness of less than around 0.5 mm, which contributes to the random texture.

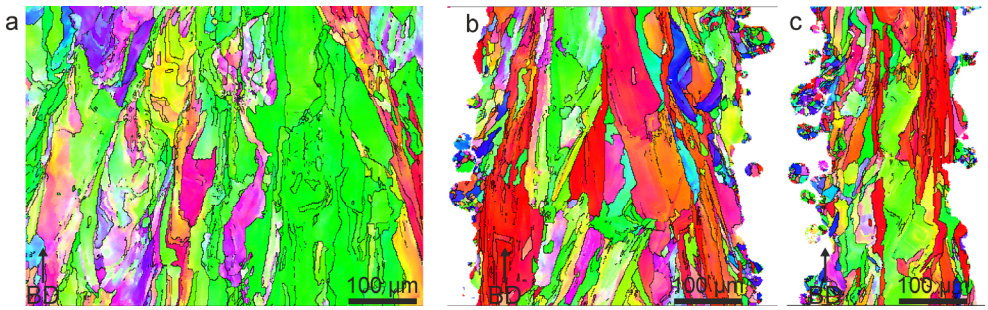


*Figure 28: EBSD orientation maps with inverse pole figure coloring of a (a) 1 mm thick rib, (b) 0.4 mm thick rib and (c) 0.2 mm thick rib.*

The cellular structure was investigated with SEM for the different thicknesses and at various locations in the samples (close to the part surface, in the center and at different build heights). However, the studies did not present any apparent differences in cell orientation, size or shape. Indeed, the variation in crystallographic orientation and grain morphology indicates differences in the solidification behavior. These differences could undoubtedly affect the cellular structure, but more dedicated studies are required to understand the effect of design at the sub-micron level.

To investigate how the part thickness affects the mechanical properties, samples with rib thicknesses of 1 and 3 mm were fabricated using standard process parameters. The dimensions of the tensile test bars are provided in **Figure 18b**. **Figure 29a** presents representative tensile curves for the two thicknesses, while **Figure 29b** displays the average tensile properties based on three tests for each thickness. It can be seen that the 1 mm thick samples exhibit lower properties with a significantly broader spread in ductility compared with the 3 mm thick sample. The lower average elongation to fracture for the 1 mm samples was partly explained by the slimness ratio [76], whereas the large spread was related to defects and surface roughness. However, defects do not significantly impact the yield strength and hence do not explain the drop in yield strength. The change in yield strength was instead explained by the generic size effect (described in detail in Section 5.3). The 3 mm thick samples exhibit similar strength and ductility as the sample with standard dimensions (**Figure 25**). Both thicknesses comply with the ASTM A240M-18 standard in terms of yield strength and ultimate tensile strength; however, the presented results imply that to correctly design and simulate mechanical properties for thin-walled components, the demonstrated size effect must be considered. In other words, the properties obtained from standard tensile bars provide an overestimated value when used for the design of thin features compared with the actual values obtained from thinner samples.

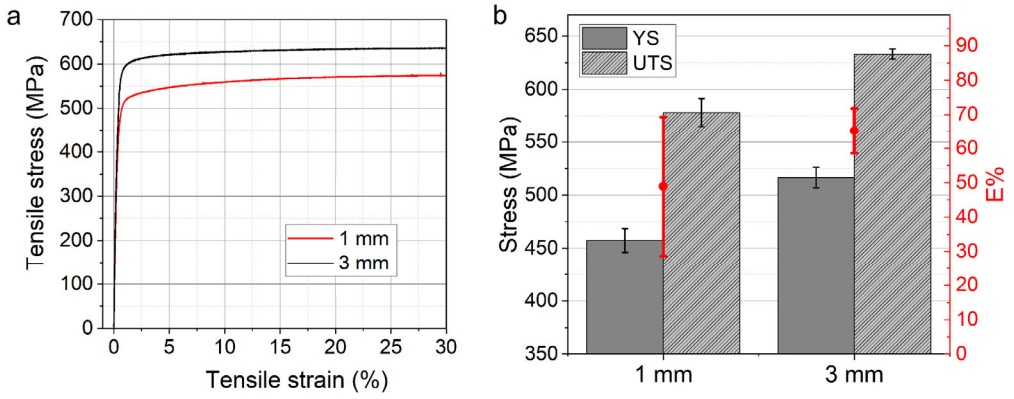


*Figure 29: Tensile properties for the part produced with different thicknesses: (a) engineering stress/strain curves and (b) the average strength and ductility generated from three different samples.*

## 7.3 Process parameters

The results presented above were obtained from parts fabricated with standard process parameters, which were developed to achieve the best performance regarding low porosity, high surface quality and high tensile properties, among others. This development is indeed essential, but to expand the L-PBF applications, further developments of the process parameters with other aims and intentions are desired. This subsection presents how the microstructure and properties can be tailored by changing some of the primary process parameters, namely the scan strategy, laser parameters (scan speed and hatch distance), layer thickness and process gas. Some of these process parameters will then be evaluated in Section 7.4 based on their effect on productivity.

### 7.3.1 Scan strategy

The standard scanning strategy for EOS M290 is bidirectional scanning (67° rotation) with a stripe pattern (as explained in Section 3.2). In this study, samples were produced without the stripe pattern and with different scan rotations (no rotation, 90°, 45° and 67°). The

microstructure of the samples produced without scan rotation is presented in **Figure 30**. As can be seen in **Figure 30a,** each melt pool is aligned in height, and inside the melts pools, a core of cells is formed with ±45° inclined cells (**Figure 30b**). The EBSD orientation map reveals large elongated grains with a strong <101> orientation separated by bands of smaller grains with a strong <001> orientation, as observable in **Figure 30c**. It is worth mentioning that the microstructures are distinctively different between all three cross-sections (see Paper IV).

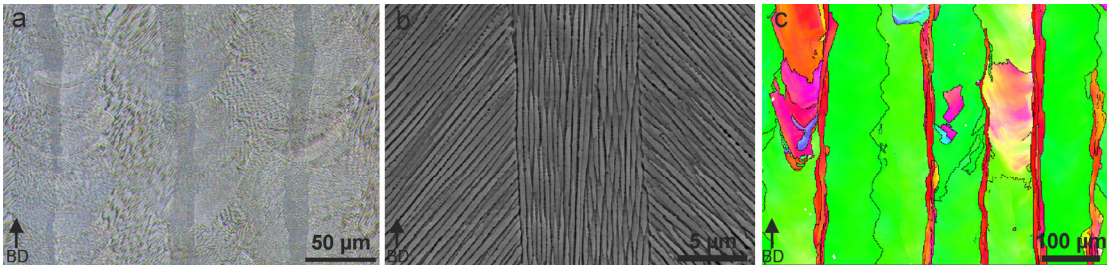


*Figure 30: Microstructure of the sample produced without scan rotation: (a) light optical image, (b) SEM image and (c) EBSD orientation map.*

**Figure 31** presents the microstructure of the sample produced with 90° scan rotations. As can be seen in **Figure 31a**, the melt pools are no longer aligned. The core of cells is replaced by a more random cell orientation, as illustrated in **Figure 31b**. The EBSD orientation map (**Figure 31c**) still presents a strong <101> orientation, but the band is no longer clearly visible. Increasing the scan rotation amplifies the complexity even further and weakens the texture intensity (still a relativity strong <101> orientation). The provided results indicate that the complex grain morphology and texture are strongly associated with the scan rotation.

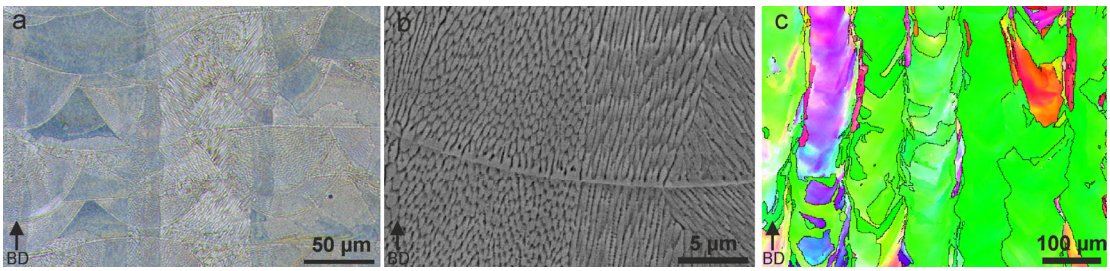


*Figure 31: Microstructure of the sample produced with a 90° scan rotation: (a) light optical image, (b) SEM image and (b) EBSD orientation map.*

The tensile properties and hardness values of the samples produced using different scan rotations are presented in **Figure 32**. The highest tensile strength was obtained from the samples produced without rotation, with a substantial increase in ductility. The hardness values presented a more homogenous result with a slight decrease for the sample produced without scan rotation. The combination of these results indicates anisotropic behavior, in which it can be expected that samples produced without scan rotation may have lower tensile properties if tested perpendicular to the building orientation.

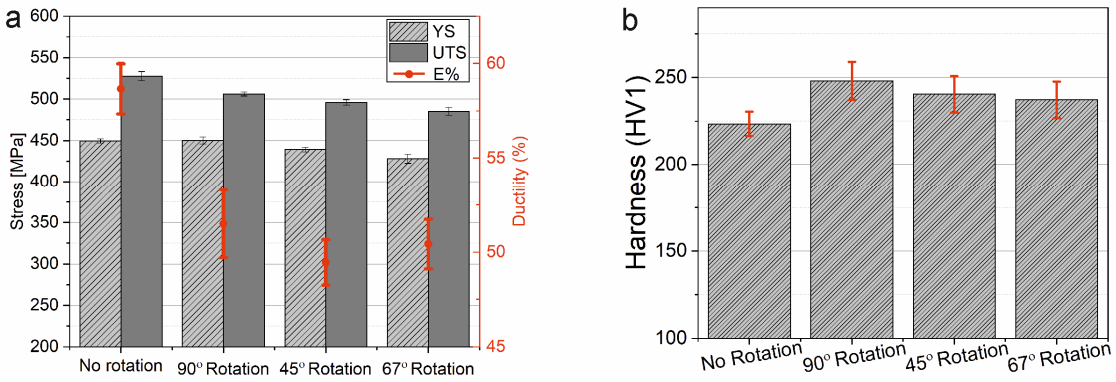


*Figure 32: Mechanical properties for the part produced with different scan rotations: (a) average strength and ductility and (b) average hardness.*

### 7.3.2 Laser-related parameters

The focus of this subsection is to elaborate on the effect of scan speed and hatch distance on the microstructure and mechanical properties. Two main challenges should be addressed when optimizing the scan speed and hatch distance; from one side, the energy density must be sufficiently high to fully melt the powder to create good adhesion between the powder layers. From the other side, the energy density should not be too high, as this might cause over-melting. Over melting could result in swelling, which could then cause the build job to fail (recoater blade might collide with the part). This is especially important when producing parts going from a thick-to-thin section. When going from a thick-to-thin section, heat accumulation increases, which increases the risk of swelling. In Paper V, the build failed when net-shaped tensile test bars were produced with higher energy densities. The failure occurred when the sample went from the gauge length to the grip head (a thin-to-thick section). To solve this, the samples were instead fabricated as rectangular plates (72x12x2.5 mm). The plates were then cut using a waterjet to generate the final dimensions, as presented in **Figure 18c**. This emphasizes the importance of considering part design and optimizing the energy density accordingly, this to increase the design capabilities.

**Figure 33** presents representative light optical micrographs of as-polished samples produced using different energy densities. As can be seen from the figure, only the samples produced with the lowest energy density present a significant number of defects, owing primarily to the lack of fusion defects. Still, the density was around 98.7%, which for some applications is still adequate.

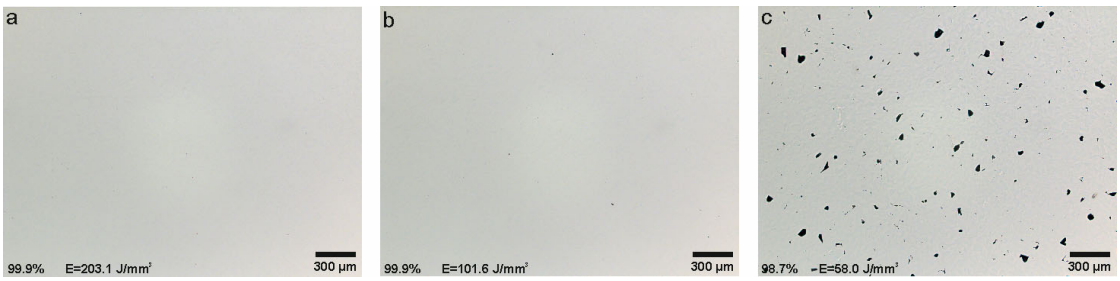


*Figure 33: Light optical micrographs of cross-sections of the parts displaying the porosity formed when using different energy densities: (a) 203.1 J/mm$^3$, (b) 101.6 J/mm$^3$ and (c) 58.0 J/mm$^3$.*

Determining grain and cell sizes in L-PBF produced samples is problematic, and the spreads are often larger than the average value. However, in this case, the process window is expressively wide, which resulted in a significant difference in both the grain size and cell size, as depicted in **Figure 34**. The samples produced with the lowest energy density exhibited nearly a 50% reduction in grain size.

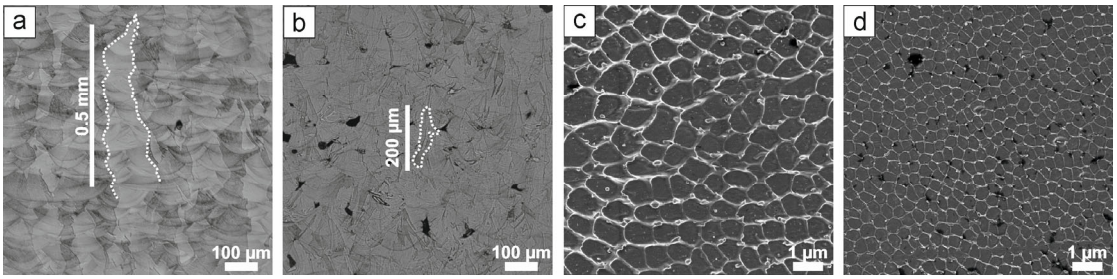


*Figure 34: Light optical images of samples produced with (a) 203 J/mm³ and (b) 58.0 J/mm³. High-magnification SEM micrographs presenting the cellular structure of samples produced with an energy density of (c) 203.1 J/mm³ and (d) 58.0 J/mm³.*

The effect of energy density was further investigated using EBSD on build samples. As presented in **Figure 35a**, the sample produced with the highest energy density consisted of large elongated grains with a very strong <101> texture, while the samples produced with the lowest energy density exhibited much smaller grains with a random texture (**Figure 35b**). It was demonstrated that the <101> preferential orientation progressively increased with increasing energy density. This can be understood by considering that a higher temperature (created by a higher energy density) generates a more uniform temperature gradient. **Figure 35c** presents the tensile properties of the samples produced with three different energy densities. Tensile testing revealed only small differences (less than 10%) in strength for the selected process parameters.

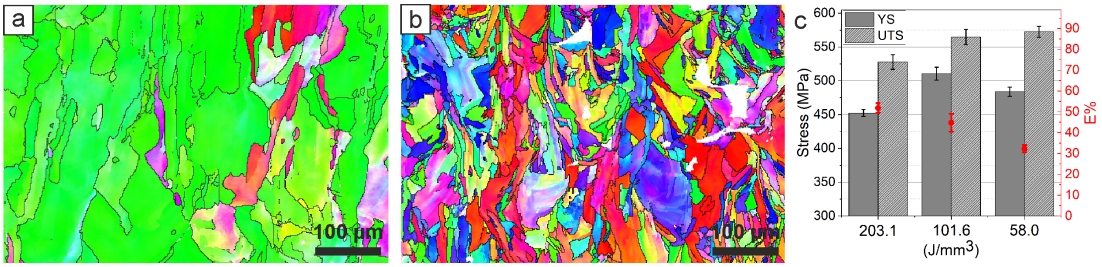


*Figure 35: EBSD orientation maps of cross-sections in building direction of the samples produced with (a) 203 J/mm³ and (b) 58.0 J/mm³. (c) Summary of tensile properties.*

### 7.3.3 Layer thickness

This investigation aimed to increase the productivity of the process by increasing the layer thickness to 80 µm. A light optical microscopy investigation revealed that the produced parts possessed high relative density (99.9%). Still, lack of fusion defects were observed in the produced parts, as illustrated in **Figure 36a.** However, the number of these defects was sufficiently small to not affect the overall density.

As observable in **Figure 36b,** the samples have significantly larger melt pools compared with the sample produced with a 20 µm layer thickness (**Figure 23b**). Furthermore, it can be seen from the EBSD orientation maps (**Figure 36c**) that the sample presents a more random

crystallographic orientation with fewer elongated grains. The grain shape is similar to the shape of the melt pools, and it appears that the grains nucleate from the melt pool boundaries.

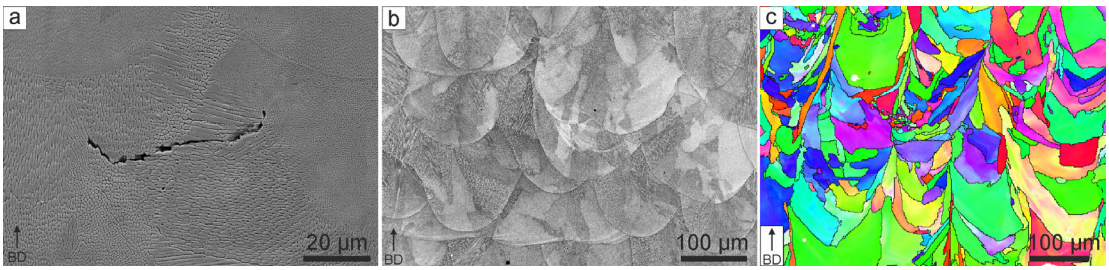


*Figure 36: (a) SEM image displays a lack of fusion defects: (b) low-magnification image of the enlarged melt pools and (c) EBSD orientation map.*

The tensile curves of the samples produced with 80 µm and 20 µm layer thickness are presented in **Figure 37**. The UTS is similar for both samples, whereas the elongation to fracture is significantly reduced for the sample produced with an 80 µm layer thickness (from 61% to 44%). This is associated with the previously observed lack of fusion defects. Furthermore, as seen from the tensile test curves, the yield strength is considerably lower for the part produced with an 80 µm layer thickness, and the sample appears to exhibit increased strain hardening. The difference was explained by disparities in dislocation density, grain size and texture.

It should be emphasized that the presented process parameters are by no means optimized. This study reveals only the potential of developing new process parameters for increased productivity. More work on improving the process parameters is necessary, especially when considering the production of parts with a build angle.

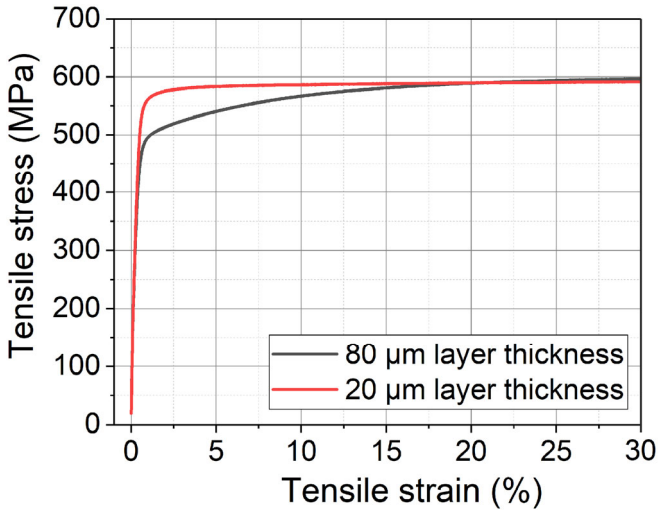


*Figure 37: Tensile test curves for the samples produced with 80µm and 20 µm layer thicknesses.*

### 7.3.4 Processing Gas

In this work, three gases were investigated: argon, nitrogen and helium. The oxygen and nitrogen contents for the samples produced using each gas in addition to the original contents of the feedstock powder are presented in **Table 3**. The nitrogen appears to be transferred to the built material, whereas a loss in oxygen is observed in the produced parts compared with the feedstock powder. This trend was observed regardless of the processing gas.

*Table 3: Contents of O and N in the powder and the 1 mm thick samples produced with different process gases.*

| Process gas | Oxygen [ppm] | Nitrogen [ppm] |
|---|---|---|
| Feedstock powder | 786 | 1240 |
| Argon | 584 | 1300 |
| Helium | 621 | 1330 |
| Nitrogen generator | 643 | 1360 |

Based on the light optical investigations, a high density (> 99.9%) was achieved for all samples regardless of the gas or the sample thickness. Furthermore, no major differences in the sample texture or grain size were observed. However, the samples produced with helium appeared to present a slightly finer cell structure, which was assumed to be associated with the higher cooling rates when using helium – due to its higher thermal conductivity – compared with argon or nitrogen.

**Figure 38** presents tensile test curves of the 3 mm thick samples produced with the three gases. A slight increase in tensile strength is observed for the samples produced with helium, which can be understood by considering the finer cell size of these samples. It has been demonstrated that helium could be successfully implemented as a potential gas for processing 316L with L-PBF. Helium might increase the capacity for heat removal and thereby reduce the risk of over-melting. The buildability of critical design features, such as parts with high aspect ratios, also increases. However, more studies are required to fully comprehend these potential buildability benefits when using helium as a process gas.

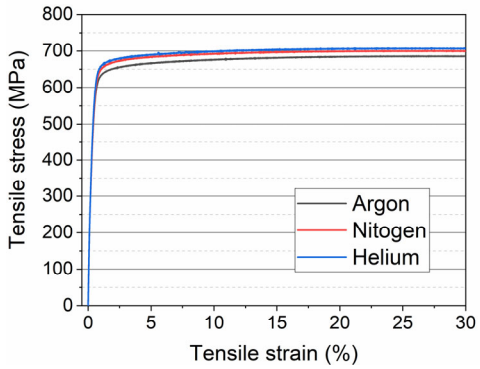


*Figure 38: Tensile test curves for samples produced with three different gases.*

## 7.4 Productivity

One of the main objectives sought by alternating the process parameters was to increase the productivity by raising the build speed. The build speed was evaluated by the volume of the material that the process could melt per time unit ($cm^3/h$). The build speed was calculated using EOS print on a build job with 250 cubes (10x10x10 $mm^3$), as illustrated in **Figure 39**. It should be noted that the build plate utilization influences the build speed value; hence, comparison between different build jobs is not applicable. However, using the same build plate utilization with different process parameters highlights the relative difference between process parameter sets. The calculated build times for some of the process parameters used in this thesis are presented in **Table 4**, which indicates that increasing the layer thickness generates the largest improvement. These results reveal that one of the main limitations of the L-PBF process – low build speed – can be significantly improved by adjusting the process parameters, without compromising the properties.

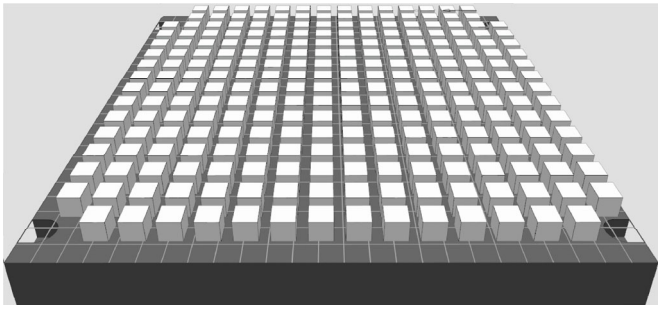

*Figure 39: Illustration of a 10x10x10 mm$^3$ cubes on a build plate prepared for calculating the build speed.*

*Table 4: The build speed of different process parameter sets based on the build plate presented in **Figure 39.***

| ID | Power | Layer thickness | Scan Speed | Hatch Distance | VED | Build Speed |
|---|---|---|---|---|---|---|
| 1 | 195 W | 0.02 mm | 800 mm/s | 0.12 mm | 101.6 J/mm$^3$ | 5.4 cm$^3$/h |
| 2 | 195 W | 0.02 mm | 1400 mm/s | 0.12 mm | 58 J/mm$^3$ | 8.2 cm$^3$/h |
| 3 | 295 W | 0.08 mm | 800 mm/s | 0.12 mm | 38.4 J/mm$^3$ | 23.2 cm$^3$/h |

## 7.5 Implementation of results

The presented research focused on the process-material-properties relationship, which is highly important in successfully increasing the industrial implementation of the L-PBF process. The purpose of this subsection is to use the conducted studies and demonstrate how the results can be implemented in a real component. The case study is used as an example of how productivity can be improved while assuring the required material properties.

The selected component was provided by Alfa Laval and is a flow connector. The component was partially redesigned and adapted for L-PBF. The isometric view of the part is presented in **Figure 40a**. The part is 260 mm in height, and the largest diameter is 70 mm, indicating that nine parts can be made per build in an EOS M290. The following calculations are based on a full build plate.

If standard process parameters with a 20 µm layer thickness are used, the build time for nine parts is approximately 458 hours. If the part is fabricated with an 80 µm layer thickness with the process parameters presented in **Table 4** (ID3), the build time is reduced to around 111 hours, a fourfold improvement.

However, it was discovered that when the part was fabricated with an 80 µm layer thickness, some design features (e.g., thick-to-thin sections) became overheated. However, the evaluation of the cubes produced with the same process parameters revealed a lack of fusion defects (Paper VI), which suggests that the energy density was on the limit to fully melt the power layers. Hence, further reducing the energy density might generate an inadequate quality. Therefore, it is suitable to use different process parameters in different areas and thereby achieve both good buildability and high productivity.

**Figure 40b** illustrates an example in which three boxes indicate areas with different requirements. The blue box indicates an area where a lower energy density is required (thin-to-thick sections). The green box indicates the most critical area where the highest ductility and yield strength are needed. Finally, the red box indicates the area with the lowest requirements, meaning that the process parameters can be selected for the highest possible productivity. The

following process parameters were used from Table 4: green box (ID1), blue box (ID2) and red box (ID3). The expected microstructures and properties of the optimized L-PBF manufacturing are presented in **Figure 40c** and are based on results obtained in the various studies provided in this thesis. A total build time of 246 hours is expected. The design could be further developed by, for example, introducing a lattice structure inside the bulk, which would reduce the build time even further. This case study demonstrated how a part could be fabricated with a pre-defined quality with area-specific requirements.

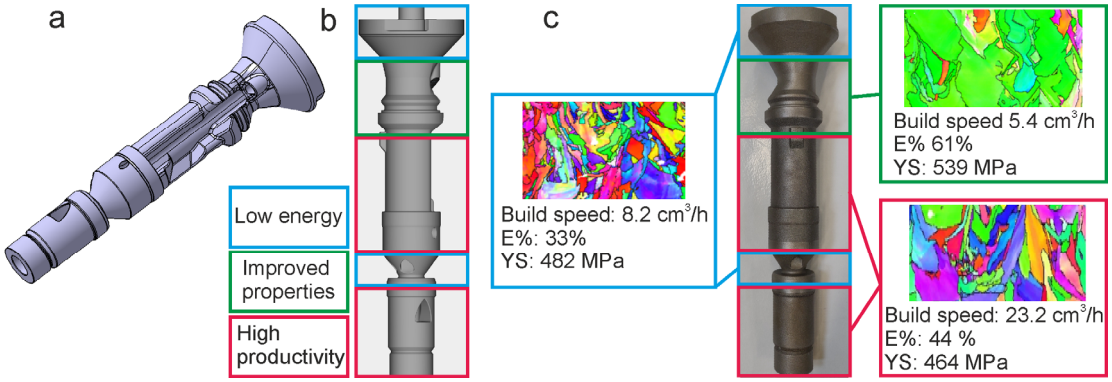


*Figure 40: A demonstrator produced by L-PBF with tailored process parameters.*

# CHAPTER 8

## CONCLUSIONS

*How does the part design affect the microstructure and mechanical properties?*

- Standard process parameters lead to excellent tensile properties and a microstructure consisting of large elongated grains with a predominant <101> orientation.
- A relative density of more than 99.9% can be realized regardless of the part thickness or build inclination.
- The thickness of a sample affects the grain morphology and texture, in which fine grains are observed close to the part edges.
- Reducing the part thickness to less than 1 mm reduces the yield strength by ~11% and increases the spread in ductility due to size and slimness effects.
- Samples with a thickness of more than 3 mm exhibit tensile properties comparable to those of the samples with standard dimensions.

*How do the processing parameters affect the microstructure and mechanical properties?*

- Crystallographic orientation and grain size can be controlled by altering the scan speed and hatch distance.
- Thin bands of small <100> oriented grains, which are surrounded by large elongated grains with a strong <101> orientation, are formed when producing samples without scan rotation. The thin bands originate from a core of cells parallel to the building direction, surrounded by cells with a ±45° inclination toward the cell core.
- Samples produced without scan rotation exhibit improved tensile properties but with increased anisotropic behavior compared with samples produced using scan rotation.
- Increasing the layer thickness to 80 µm results in a random texture with less elongated grains and with a yield strength reduced by ~14% and elongation to fracture reduced by ~30%.
- The microstructure, tensile strength and hardness are not significantly affected by the process gas composition (helium, nitrogen and argon).

*How can productivity be improved without compromising the mechanical properties?*

- A 20% faster built time can be achieved by adjusting the scan speed and hatch distance without significantly affecting the static properties.
- Increasing the layer thickness from 20 µm to 80 µm allows for shortening the build time by a factor of four but with some reduction in yield strength and ductility.

# CHAPTER 9

## FUTURE WORK

Based on the presented results and conclusions, the following recommendations are suggested to improve the L-PBF processing of stainless steel 316L:

- The strengthening and deformation mechanisms must be studied further in relation to the submicron cellular microstructure, which requires more dedicated, high-resolution characterization techniques.
- Reproducibility of the results in dependence on the hardware and hence the process parameters must be systematically studied.
- Further possibilities to expand the L-PBF process window should be evaluated to improve the productivity even further.
- The critical part thickness for L-PBF produced samples was presented for one build direction. However, this size effect should be subjected to future examination with respect to the effect of build orientation to determine the proper design parameters.
- Further process development for the fabrication of components made with an 80 µm layer thickness must be addressed, with a focus on the improvement of the surface roughness of overhangs, among others.
- The provided results demonstrated that helium could be implemented as a process gas. This should be investigated further to increase the productivity.
- Dynamic mechanical properties should be studied, especially regarding the processes aiming for higher build speed.

# CHAPTER 10

## ACKNOWLEDGMENTS

I wish to express my gratitude to my main supervisor, Prof. Eduard Hryha, for guidance and for providing me the opportunity to work with this rapidly growing and exciting topic. In addition, I would like to extend that gratitude to my co-supervisor, Prof. Uta Klement, for offering input and guidance throughout this journey; a special thanks should be given for the endless patience provided regarding my EBSD struggles. Thank you also to my examiner, Prof. Lars Nyborg, for providing support and feedback and for all the discussions. Moreover, I would like to offer my appreciation to Christer Persson for our fruitful discussions regarding the mechanical properties and for the enjoyable off-topic discussions over the weekends.

This work was completed in the frame of the Centre for Additive Manufacturing—Metal ($CAM^2$), supported by the Swedish Governmental Agency of Innovation Systems (Vinnova). Part of this work was conducted within the project "Additive Manufacturing using Metal Pilot Line, Manuela" through funding from the European Union's Horizon 2020 Research and Innovation Programme under grain agreement no. 820774. The further financial support provided by Fusion for Energy through the grant GRT-645, (Västragötalandsregionen and Tillväxtverket) and AMLIGHT project within the Innovation Programme Metallic Materials, supported by Vinnova, Formas och Energimyndigheten, is gratefully acknowledged.

Furthermore, I would like to acknowledge Dr. Ruslan Shvab, Dr. Eric Tam, Dr. Yiming Yao, Dr. Yu Cao, Roger Sagdahl, Lic. Eng. Adrianna Lozinko and Håkan Millqvist for all their practical help.

I would also like to extend my recognition to all the colleagues at the Department of Industrial and Materials Science for making my time at the department enjoyable. In addition, a special thanks should be given to Camille, Dmitri, Eric, Hans and Johan for all the discussion, ideas and memorable stories created during our conferences.

I would like to thank my lovely family for your unconditional love and support. To my wonderful parents and sisters (and, of course, your families), I feel blessed to have you in my life. I show special gratitude to my mother for taking care of Edvin during the weekends and for all the love you gave him during this time.

To Linn, I thank you for all the support you have provided during my difficult times, for your endless love, for taking care of our children and for lighting up my life. It is now time to move on, to explore the next chapter together as a family.

Finally, to Edvin and Ines, our babies, I thank you for all your joy and love, for all your strength, and for teaching me more than any education could.

# CHAPTER 11

## REFERENCES


[1] Z. Xiao, Y. Yang, R. Xiao, Y. Bai, C. Song, D. Wang, Evaluation of topology-optimized lattice structures manufactured via selective laser melting, Mater. Des. 143 (2018) 27–37. doi:10.1016/j.matdes.2018.01.023.

[2] Y.M. Wang, T. Voisin, J.T. McKeown, J. Ye, N.P. Calta, Z. Li, Z. Zeng, Y. Zhang, W. Chen, T.T. Roehling, R.T. Ott, M.K. Santala, P.J.J.J. Depond, M.J. Matthews, A. V. Hamza, T. Zhu, Additively manufactured hierarchical stainless steels with high strength and ductility, Nat. Mater. 17 (2018) 63–70. doi:10.1038/NMAT5021.

[3] W.M. Tucho, V.H. Lysne, H. Austbø, A. Sjolyst-Kverneland, V. Hansen, Investigation of effects of process parameters on microstructure and hardness of SLM manufactured SS316L, J. Alloys Compd. 740 (2018) 910–925. doi:10.1016/j.jallcom.2018.01.098.

[4] O.O. Salman, F. Brenne, T. Niendorf, J. Eckert, K.G. Prashanth, T. He, S. Scudino, Impact of the scanning strategy on the mechanical behavior of 316L steel synthesized by selective laser melting, J. Manuf. Process. 45 (2019) 255–261. doi:10.1016/j.jmapro.2019.07.010.

[5] R.R. Dehoff, M.M. Kirka, W.J. Sames, H. Bilheux, A.S. Tremsin, L.E. Lowe, S.S. Babu, Site specific control of crystallographic grain orientation through electron beam additive manufacturing, Mater. Sci. Technol. 31 (2015) 931–938. doi:10.1179/1743284714Y.0000000734.

[6] F. Geiger, K. Kunze, T. Etter, Tailoring the texture of IN738LC processed by selective laser melting (SLM) by specific scanning strategies, Mater. Sci. Eng. A. 661 (2016) 240–246. doi:10.1016/j.msea.2016.03.036.

[7] T. Niendorf, S. Leuders, A. Riemer, F. Brenne, T. Tröster, H.A. Richard, D. Schwarze, Functionally graded alloys obtained by additive manufacturing, Adv. Eng. Mater. 16 (2014) 857–861. doi:10.1002/adem.201300579.

[8] A. Leicht, M. Rashidi, U. Klement, E. Hryha, A. Leicht; M. Rashidi; U. Klement; E. Hryha, A. Leicht, M. Rashidi, U. Klement, E. Hryha, A. Leicht; M. Rashidi; U. Klement; E. Hryha, A. Leicht, M. Rashidi, U. Klement, E. Hryha, Effect of process parameters on the microstructure, tensile strength and productivity of 316L parts produced by laser powder bed fusion, Mater. Charact. (2020) 110016. doi:10.1016/j.matchar.2019.110016.

[9] M. Schmidt, M. Merklein, D. Bourell, D. Dimitrov, T. Hausotte, K. Wegener, L. Overmeyer, F. Vollertsen, G.N. Levy, Laser based additive manufacturing in industry and academia, CIRP Ann. 66 (2017) 561–583. doi:10.1016/j.cirp.2017.05.011.

[10] Introduction to Additive Manufacturing Technology, EPMA. (2019). www.epma.com/am.

[11] ASTM International, F2792-12a - Standard Terminology for Additive Manufacturing Technologies, 2013. doi:10.1007/978-1-4419-1120-9.

[12] C. Culmone, G. Smit, P. Breedveld, Additive manufacturing of medical instruments: A state-of-the-art review, Addit. Manuf. 27 (2019) 461–473. doi:10.1016/j.addma.2019.03.015.

[13] M. Attaran, The rise of 3-D printing: The advantages of additive manufacturing over traditional manufacturing, Bus. Horiz. 60 (2017) 677–688. doi:10.1016/j.bushor.2017.05.011.

[14] C. Boig, M. Burkinshaw, C. Boig, I. Todd, The application of additive manufacturing to turbomachinery, Inst. Mech. Eng. - 13th Int. Conf. Turbochargers Turbocharging 2018. (2018) 261–269.

[15] Z.C. Oter, M. Coskun, Y. Akca, Ö. Sürmen, M.S. Yılmaz, G. Özer, G. Tarakçı, E. Koc, Benefits of laser beam based additive manufacturing in die production, Optik (Stuttg). 176 (2019) 175–184. doi:10.1016/j.ijleo.2018.09.079.

[16] D. Gu, Laser Additive Manufacturing of High-Performance Materials, n.d.

[17] O. Diegel, A. Nordin, D. Motte, A Practical Guide to Design for Additive Manufacturing, 2019. doi:10.1007/978-981-13-8281-9.

[18] M.S.F. de Lima, S. Sankaré, Microstructure and mechanical behavior of laser additive manufactured AISI 316 stainless steel stringers, Mater. Des. 55 (2014) 526–532. doi:10.1016/j.matdes.2013.10.016.

[19] G. Miranda, S. Faria, F. Bartolomeu, E. Pinto, S. Madeira, A. Mateus, P. Carreira, N. Alves, F.S. Silva, O. Carvalho, Predictive models for physical and mechanical properties of 316L stainless steel produced by selective laser melting, Mater. Sci. Eng. A. 657 (2016) 43–56. doi:10.1016/j.msea.2016.01.028.

[20] P. Hanzl, M. Zetek, T. Bakša, T. Kroupa, The influence of processing parameters on the mechanical properties of SLM parts, Procedia Eng. 100 (2015) 1405–1413. doi:10.1016/j.proeng.2015.01.510.

[21] W. Qingsong, L. Shuai, H. Changjun, L. Wei, C. Lingyu, H. Liang, S. Yusheng, Selective laser melting of stainless-steel/nano-hydroxyapatite composites for medical applications: microstructure, element distribution, crack and mechanical properties, J. Mater. Process. Technol. 222 (2015) 444–453. doi:10.1016/j.jmatprotec.2015.02.010.

[22] I. Tolosa, F. Garciandía, F. Zubiri, F. Zapirain, A. Esnaola, Study of mechanical properties of AISI 316 stainless steel processed by “selective laser melting”, following different manufacturing strategies, Int. J. Adv. Manuf. Technol. 51 (2010) 639–647. doi:10.1007/s00170-010-2631-5.

[23] W.E. King, H.D. Barth, V.M. Castillo, G.F. Gallegos, J.W. Gibbs, D.E. Hahn, C. Kamath, A.M. Rubenchik, Observation of keyhole-mode laser melting in laser powder-bed fusion additive manufacturing, J. Mater. Process. Technol. 214 (2014) 2915–2925. doi:10.1016/j.jmatprotec.2014.06.005.

[24] Z. Sun, X. Tan, S.B. Tor, C.K. Chua, Simultaneously enhanced strength and ductility for 3D-printed stainless steel 316L by selective laser melting, NPG Asia Mater. 10 (2018) 127–136. doi:10.1038/s41427-018-0018-5.

[25] S.-H. Sun, T. Ishimoto, K. Hagihara, Y. Tsutsumi, T. Hanawa, T. Nakano, Excellent mechanical and corrosion properties of austenitic stainless steel with a unique crystallographic lamellar microstructure via selective laser melting, Scr. Mater. 159

(2019) 89–93. doi:10.1016/j.scriptamat.2018.09.017.

[26] I. Yadroitsev, P. Krakhmalev, I. Yadroitsava, S. Johansson, I. Smurov, Energy input effect on morphology and microstructure of selective laser melting single track from metallic powder, J. Mater. Process. Technol. 213 (2013) 606–613. doi:10.1016/j.jmatprotec.2012.11.014.

[27] J.D. Majumdar, A. Pinkerton, Z. Liu, I. Manna, L. Li, Microstructure characterisation and process optimization of laser assisted rapid fabrication of 316L stainless steel, Appl. Surf. Sci. 247 (2005) 320–327. doi:10.1016/j.apsusc.2005.01.039.

[28] E. Yasa, J.-P.P. Kruth, Microstructural investigation of selective laser melting 316L stainless steel parts exposed to laser re-melting, Procedia Eng. 19 (2011) 389–395. doi:10.1016/j.proeng.2011.11.130.

[29] A.I. Mertens, S. Reginster, Q. Contrepois, T. Dormal, O. Lemaire, J. Lecomte-Beckers, Mechanical properties of alloy Ti–6Al–4V and of stainless steel 316L processed by selective laser melting: influence of out-of-equilibrium microstructures, Mater. Sci. Forum. 783–786 (2014) 898–903. doi:10.4028/www.scientific.net/MSF.783-786.898.

[30] Y. Zhong, L. Liu, S. Wikman, D. Cui, Z. Shen, Intragranular cellular segregation network structure strengthening 316L stainless steel prepared by selective laser melting, J. Nucl. Mater. 470 (2016) 170–178. doi:10.1016/j.jnucmat.2015.12.034.

[31] S.H. Sun, K. Hagihara, T. Nakano, Effect of scanning strategy on texture formation in Ni-25 at.%Mo alloys fabricated by selective laser melting, Mater. Des. 140 (2018) 307–316. doi:10.1016/j.matdes.2017.11.060.

[32] M.L. Montero-Sistiaga, M. Godino-Martinez, K. Boschmans, J.P. Kruth, J. Van Humbeeck, K. Vanmeensel, Microstructure evolution of 316L produced by HP-SLM (high power selective laser melting), Addit. Manuf. 23 (2018) 402–410. doi:10.1016/j.addma.2018.08.028.

[33] B. AlMangour, D. Grzesiak, J.M. Yang, Scanning strategies for texture and anisotropy tailoring during selective laser melting of TiC/316L stainless steel nanocomposites, J. Alloys Compd. 728 (2017) 424–435. doi:10.1016/j.jallcom.2017.08.022.

[34] J. Suryawanshi, K.G. Prashanth, U. Ramamurty, Mechanical behavior of selective laser melted 316L stainless steel, Mater. Sci. Eng. A. 696 (2017) 113–121. doi:10.1016/j.msea.2017.04.058.

[35] X. Zhou, K. Li, D. Zhang, X. Liu, J. Ma, W. Liu, Z. Shen, Textures formed in a CoCrMo alloy by selective laser melting, J. Alloys Compd. 631 (2015) 153–164. doi:10.1016/j.jallcom.2015.01.096.

[36] J. Robinson, I. Ashton, P. Fox, E. Jones, C. Sutcliffe, Determination of the effect of scan strategy on residual stress in laser powder bed fusion additive manufacturing, Addit. Manuf. 23 (2018) 13–24. doi:10.1016/j.addma.2018.07.001.

[37] H. Ali, H. Ghadbeigi, K. Mumtaz, Effect of scanning strategies on residual stress and mechanical properties of Selective Laser Melted Ti6Al4V, Mater. Sci. Eng. A. 712 (2018) 175–187. doi:10.1016/j.msea.2017.11.103.

[38] J.A. Pakkanen, Designing for Additive Manufacturing-Product and Process Driven Design for Metals and Polymers, 2018. doi:10.6092/polito/porto/2714732.

[39] J.L. Bartlett, X. Li, An overview of residual stresses in metal powder bed fusion, Addit. Manuf. 27 (2019) 131–149. doi:10.1016/j.addma.2019.02.020.

[40] I. Koutiri, E. Pessard, P. Peyre, O. Amlou, T. De Terris, Influence of SLM process parameters on the surface finish, porosity rate and fatigue behavior of as-built Inconel 625 parts, J. Mater. Process. Technol. 255 (2018) 536–546. doi:10.1016/j.jmatprotec.2017.12.043.

[41] E. Hryha, R. Shvab, H. Gruber, A. Leicht, L. Nyborg, Surface Oxide State on Metal Powder and its Changes during Additive Manufacturing : an Overview, La Metall. Ital. (2018) 34–39.

[42] C. Pauzon, E. Hryha, P. Forêt, L. Nyborg, Effect of argon and nitrogen atmospheres on the properties of stainless steel 316L parts produced by laser-powder bed fusion, Mater. Des. (2019) 107873. doi:10.1016/j.matdes.2019.107873.

[43] C. Pauzon, The Process Atmosphere as a Parameter in the Laser-Powder Bed Fusion Process, (2019).

[44] C. Pauzon, E. Hryha, P. Forêt, L. Nyborg, Effect of argon and nitrogen atmospheres on the properties of stainless steel 316 L parts produced by laser-powder bed fusion, Mater. Des. 179 (2019). doi:10.1016/j.matdes.2019.107873.

[45] D. Wang, S. Mai, D. Xiao, Y. Yang, Surface quality of the curved overhanging structure manufactured from 316-L stainless steel by SLM, Int. J. Adv. Manuf. Technol. 86 (2016) 781–792. doi:10.1007/s00170-015-8216-6.

[46] Y.J. Yin, J.Q. Sun, J. Guo, X.F. Kan, D.C. Yang, Mechanism of high yield strength and yield ratio of 316 L stainless steel by additive manufacturing, Mater. Sci. Eng. A. 744 (2019) 773–777. doi:10.1016/j.msea.2018.12.092.

[47] E. Liverani, S. Toschi, L. Ceschini, A. Fortunato, Effect of selective laser melting (SLM) process parameters on microstructure and mechanical properties of 316L austenitic stainless steel, J. Mater. Process. Technol. 249 (2017) 255–263. doi:10.1016/j.jmatprotec.2017.05.042.

[48] K. Saeidi, X. Gao, F. Lofaj, L. Kvetková, Z.J.J. Shen, Transformation of austenite to duplex austenite-ferrite assembly in annealed stainless steel 316L consolidated by laser melting, J. Alloys Compd. 633 (2015) 463–469. doi:10.1016/j.jallcom.2015.01.249.

[49] M. Rombouts, Selective Laser Sintering / Melting of Iron-Based Powders, PhD Thesis Kathol. Univ. Leuven. (2006). doi:10.2143/SDL.46.3.2004771.

[50] D. Wang, C. Song, Y. Yang, Y. Bai, Investigation of crystal growth mechanism during selective laser melting and mechanical property characterization of 316L stainless steel parts, Mater. Des. 100 (2016) 291–299. doi:10.1016/j.matdes.2016.03.111.

[51] X. Wang, J.A. Muñiz-Lerma, O. Sánchez-Mata, M. Attarian Shandiz, M. Brochu, Microstructure and mechanical properties of stainless steel 316L vertical struts manufactured by laser powder bed fusion process, Mater. Sci. Eng. A. 736 (2018) 27–40. doi:10.1016/j.msea.2018.08.069.

[52] K. Saeidi, X. Gao, Y. Zhong, Z.J.J. Shen, Hardened austenite steel with columnar sub-grain structure formed by laser melting, Mater. Sci. Eng. A. 625 (2015) 221–229. doi:10.1016/j.msea.2014.12.018.

[53] R. Casati, J. Lemke, M. Vedani, Microstructure and Fracture Behavior of 316L Austenitic Stainless Steel Produced by Selective Laser Melting, J. Mater. Sci. Technol. 32 (2016) 738–744. doi:10.1016/j.jmst.2016.06.016.

[54] Z. Sun, X. Tan, S.B. Tor, W.Y. Yeong, Selective laser melting of stainless steel 316L with low porosity and high build rates, Mater. Des. 104 (2016) 197–204.

doi:10.1016/j.matdes.2016.05.035.

[55] Y.D. Im, K.H. Kim, K.H. Jung, Y.K. Lee, K.H. Song, Anisotropic Mechanical Behavior of Additive Manufactured AISI 316L Steel, Metall. Mater. Trans. A Phys. Metall. Mater. Sci. 50 (2019) 2014–2021. doi:10.1007/s11661-019-05139-7.

[56] A. Leicht, U. Klement, E. Hryha, Effect of build geometry on the microstructural development of 316L parts produced by additive manufacturing, Mater. Charact. 143 (2018) 137–143. doi:10.1016/j.matchar.2018.04.040.

[57] T. Niendorf, S. Leuders, A. Riemer, H.A. Richard, T. Tröster, D. Schwarze, Highly anisotropic steel processed by selective laser melting, Metall. Mater. Trans. B Process Metall. Mater. Process. Sci. 44 (2013) 794–796. doi:10.1007/s11663-013-9875-z.

[58] S. Leuders, M. Thöne, a. Riemer, T. Niendorf, T. Tröster, H. a. Richard, H.J. Maier, On the mechanical behaviour of titanium alloy TiAl6V4 manufactured by selective laser melting: Fatigue resistance and crack growth performance, Int. J. Fatigue. 48 (2013) 300–307. doi:10.1016/j.ijfatigue.2012.11.011.

[59] O. Andreau, I. Koutiri, P. Peyre, J.D. Penot, N. Saintier, E. Pessard, T. De Terris, C. Dupuy, T. Baudin, Texture control of 316L parts by modulation of the melt pool morphology in selective laser melting, J. Mater. Process. Technol. 264 (2019) 21–31. doi:10.1016/j.jmatprotec.2018.08.049.

[60] a. a. Antonysamy, J. Meyer, P.B. Prangnell, Effect of build geometry on the β-grain structure and texture in additive manufacture of Ti6Al4V by selective electron beam melting, Mater. Charact. 84 (2013) 153–168. doi:10.1016/j.matchar.2013.07.012.

[61] M.C.F. T. F. Bower, Structure of dendrites at chill surfaces, Trans. Met. Soc. AIME. 239 (1967) 1620–1625.

[62] J.R. Davis, ASM International. Handbook Committee., Stainless steels, ASM International, 1994.

[63] EOS, Material data sheet - EOS StainlessSteel 316L, 49 (2014) 1–5.

[64] K. Lu, K. Lu, L. Lu, S. Suresh, Strengthening Materials by Boundaries at the Nanoscale, Science (80-. ). 349 (2009) 349–353. doi:10.1126/science.1159610.

[65] K. Obrtlík, T. Kruml, J. Polák, Dislocation structures in 316L stainless steel cycled with plastic strain amplitudes over a wide interval, Mater. Sci. Eng. A. 187 (1994) 1–9. doi:10.1016/0921-5093(94)90325-5.

[66] R. Dmitri, B. Sven, Factors Affecting Printability of 316L Powders Using the DMLS Process, WorldPM 2018. (2018) 1640–1649.

[67] B.C. De Cooman, Y. Estrin, S.K. Kim, Twinning-induced plasticity (TWIP) steels, Acta Mater. 142 (2018) 283–362. doi:10.1016/j.actamat.2017.06.046.

[68] S. Sinha, J.A. Szpunar, N.A.P. Kiran Kumar, N.P. Gurao, Tensile deformation of 316L austenitic stainless steel using in-situ electron backscatter diffraction and crystal plasticity simulations, Mater. Sci. Eng. A. 637 (2015) 48–55. doi:10.1016/j.msea.2015.04.005.

[69] M.W. Fu, W.L. Chan, Micro-scaled products development via microforming : deformation behaviours, processes, tooling and its realization, 2014. https://books.google.com/books?id=Yie_BAAAQBAJ&pg=PA100.

[70] A. Kohyama, K. Hamada, H. Matsui, Specimen size effects on tensile properties of neutron-irradiated steels, J. Nucl. Mater. 179–181 (1991) 417–420. doi:10.1016/0022-

3115(91)90113-L.

[71] R.W. Armstrong, On size effects in polycrystal plasticity, J. Mech. Phys. Solids. 9 (1961) 196–199. doi:10.1016/0022-5096(61)90018-7.

[72] M.W. Fu, W.L. Chan, Geometry and grain size effects on the fracture behavior of sheet metal in micro-scale plastic deformation, Mater. Des. 32 (2011) 4738–4746. doi:10.1016/j.matdes.2011.06.039.

[73] A. Diehl, U. Engel, M. Geiger, Influence of microstructure on the mechanical properties and the forming behaviour of very thin metal foils, Int. J. Adv. Manuf. Technol. 47 (2010) 53–61. doi:10.1007/s00170-008-1851-4.

[74] L. V. Raulea, A.M. Goijaerts, L.E. Govaert, F.P.T. Baaijens, Size effects in the processing of thin metal sheets, J. Mater. Process. Technol. 115 (2001) 44–48. doi:10.1016/S0924-0136(01)00770-1.

[75] W.L. Chan, M.W. Fu, Experimental studies and numerical modeling of the specimen and grain size effects on the flow stress of sheet metal in microforming, Mater. Sci. Eng. A. 528 (2011) 7674–7683. doi:10.1016/j.msea.2011.06.076.

[76] ASM International. Handbook Committee, ASM Handb. Mech. Test. Eval. 8 (2000). www.asminternational.org.

[77] W. Shifeng, L. Shuai, W. Qingsong, C. Yan, Z. Sheng, S. Yusheng, Effect of molten pool boundaries on the mechanical properties of selective laser melting parts, J. Mater. Process. Technol. 214 (2014) 2660–2667. doi:10.1016/j.jmatprotec.2014.06.002.

[78] A. Röttger, K. Geenen, M. Windmann, F. Binner, W. Theisen, Comparison of microstructure and mechanical properties of 316 L austenitic steel processed by selective laser melting with hot-isostatic pressed and cast material, Mater. Sci. Eng. A. 678 (2016) 365–376. doi:10.1016/j.msea.2016.10.012.

[79] D. Wang, Y. Yang, X. Su, Y. Chen, Study on energy input and its influences on single-track,multi-track, and multi-layer in SLM, Int. J. Adv. Manuf. Technol. 58 (2012) 1189–1199. doi:10.1007/s00170-011-3443-y.

[80] M.S. Pham, B. Dovgyy, P.A. Hooper, Twinning induced plasticity in austenitic stainless steel 316L made by additive manufacturing, Mater. Sci. Eng. A. 704 (2017) 102–111. doi:10.1016/j.msea.2017.07.082.

[81] K. Saeidi, L. Kvetková, F. Lofaj, Z. Shen, Austenitic stainless steel strengthened by the in situ formation of oxide nanoinclusions, RSC Adv. 5 (2015) 20747–20750. doi:10.1039/c4ra16721j.

[82] L. Liu, Q. Ding, Y. Zhong, J. Zou, J. Wu, Y.L. Chiu, J. Li, Z. Zhang, Q. Yu, Z. Shen, Dislocation network in additive manufactured steel breaks strength–ductility trade-off, Mater. Today. 21 (2018) 354–361. doi:10.1016/j.mattod.2017.11.004.

[83] C.A. Schneider, W.S. Rasband, K.W. Eliceiri, NIH Image to ImageJ: 25 years of image analysis, Nat. Methods. 9 (2012) 671–675. doi:10.1038/nmeth.2089.

[84] Knowles, Crystallography and Crystal Defects, 2th ed., New York: Wiley, 2000.

[85] J. Pešička, R. Kužel, A. Dronhofer, G. Eggeler, The evolution of dislocation density during heat treatment and creep of tempered martensite ferritic steels, Acta Mater. 51 (2003) 4847–4862. doi:10.1016/S1359-6454(03)00324-0.

[86] F. Stern, J. Kleinhorst, J. Tenkamp, F. Walther, Investigation of the anisotropic cyclic damage behavior of selective laser melted AISI 316L stainless steel, Fatigue Fract.

Eng. Mater. Struct. 7 (2019) 1–9. doi:10.1111/ffe.13029.

[87] L.H. Hamza Hassn Alsalla, Christopher Smith, Effect of build orientation on the surface quality, microstructure and mechanical properties of selective laser melting 316L stainless steel, Rapid Prototyp. J. 24 (2018) 9–17. doi:https://doi.org/10.1108/RPJ-04-2016-0068.

[88] Y.N. Zhang, X. Cao, P. Wanjara, M. Medraj, Oxide films in laser additive manufactured Inconel 718, Acta Mater. 61 (2013) 6562–6576. doi:10.1016/j.actamat.2013.07.039.